

*Suzaku* Observations of Luminous Quasars:  
Revealing the Nature of High-Energy Blazar Emission  
in Low-level activity States

A. A. Abdo<sup>1,2</sup>, M. Ackermann<sup>3</sup>, M. Ajello<sup>3</sup>, E. Antolini<sup>4,5</sup>, L. Baldini<sup>6</sup>, J. Ballet<sup>7</sup>,  
G. Barbiellini<sup>8,9</sup>, M. G. Baring<sup>10</sup>, D. Bastieri<sup>11,12</sup>, K. Bechtol<sup>3</sup>, R. Bellazzini<sup>6</sup>, B. Berenji<sup>3</sup>,  
R. D. Blandford<sup>3</sup>, E. D. Bloom<sup>3</sup>, E. Bonamente<sup>4,5</sup>, A. W. Borgland<sup>3</sup>, J. Bregeon<sup>6</sup>, A. Brez<sup>6</sup>,  
M. Brigida<sup>13,14</sup>, P. Bruel<sup>15</sup>, R. Buehler<sup>3</sup>, S. Buson<sup>11</sup>, G. A. Caliandro<sup>16</sup>, R. A. Cameron<sup>3</sup>,  
S. Carrigan<sup>12</sup>, J. M. Casandjian<sup>7</sup>, E. Cavazzuti<sup>17</sup>, C. Cecchi<sup>4,5</sup>, Ö. Çelik<sup>18,19,20</sup>,  
A. Chekhtman<sup>1,21</sup>, A. W. Chen<sup>22</sup>, J. Chiang<sup>3</sup>, S. Ciprini<sup>5</sup>, R. Claus<sup>3</sup>, J. Cohen-Tanugi<sup>23</sup>,  
S. Colafrancesco<sup>17</sup>, J. Conrad<sup>24,25,26</sup>, S. Cutini<sup>17</sup>, C. D. Dermer<sup>1</sup>, F. de Palma<sup>13,14</sup>,  
S. W. Digel<sup>3</sup>, E. do Couto e Silva<sup>3</sup>, P. S. Drell<sup>3</sup>, R. Dubois<sup>3</sup>, D. Dumora<sup>27,28</sup>, C. Farnier<sup>23</sup>,  
C. Favuzzi<sup>13,14</sup>, S. J. Fegan<sup>15</sup>, E. C. Ferrara<sup>18</sup>, W. B. Focke<sup>3</sup>, M. Frailis<sup>29,30</sup>, Y. Fukazawa<sup>31</sup>,  
P. Fusco<sup>13,14</sup>, F. Gargano<sup>14</sup>, D. Gasparri<sup>17</sup>, N. Gehrels<sup>18</sup>, B. Giebels<sup>15</sup>, N. Giglietto<sup>13,14</sup>,  
P. Giommi<sup>17</sup>, F. Giordano<sup>13,14</sup>, M. Giroletti<sup>32</sup>, T. Glanzman<sup>3</sup>, G. Godfrey<sup>3</sup>, P. Grandi<sup>33</sup>,  
I. A. Grenier<sup>7</sup>, L. Guillemot<sup>34,27,28</sup>, S. Guiriec<sup>35</sup>, D. Hadasch<sup>36</sup>, A. K. Harding<sup>18</sup>,  
M. Hayashida<sup>3</sup>, D. Horan<sup>15</sup>, R. E. Hughes<sup>37</sup>, R. Itoh<sup>31</sup>, M. S. Jackson<sup>38,25</sup>, G. Jóhannesson<sup>3</sup>,  
A. S. Johnson<sup>3</sup>, W. N. Johnson<sup>1</sup>, T. Kamae<sup>3</sup>, H. Katagiri<sup>31</sup>, J. Kataoka<sup>39</sup>, N. Kawai<sup>40,41</sup>,  
J. Knödlseeder<sup>42</sup>, M. Kuss<sup>6</sup>, J. Lande<sup>3</sup>, L. Latronico<sup>6</sup>, F. Longo<sup>8,9</sup>, F. Loparco<sup>13,14</sup>,  
B. Lott<sup>27,28</sup>, M. N. Lovellette<sup>1</sup>, P. Lubrano<sup>4,5</sup>, G. M. Madejski<sup>3</sup>, A. Makeev<sup>1,21</sup>,  
M. N. Mazziotta<sup>14</sup>, J. E. McEnery<sup>18,43</sup>, S. McGlynn<sup>38,25</sup>, C. Meurer<sup>24,25</sup>, P. F. Michelson<sup>3</sup>,  
W. Mitthumsiri<sup>3</sup>, T. Mizuno<sup>31</sup>, C. Monte<sup>13,14</sup>, M. E. Monzani<sup>3</sup>, A. Morselli<sup>44</sup>,  
I. V. Moskalenko<sup>3</sup>, S. Murgia<sup>3</sup>, I. Nestoras<sup>34</sup>, P. L. Nolan<sup>3</sup>, J. P. Norris<sup>45</sup>, E. Nuss<sup>23</sup>,  
T. Ohsugi<sup>46</sup>, A. Okumura<sup>47</sup>, E. Orlando<sup>48</sup>, J. F. Ormes<sup>45</sup>, M. Ozaki<sup>49</sup>, D. Paneque<sup>3</sup>,  
J. H. Panetta<sup>3</sup>, D. Parent<sup>1,21,27,28</sup>, V. Pelassa<sup>23</sup>, M. Pepe<sup>4,5</sup>, M. Pesce-Rollins<sup>6</sup>, F. Piron<sup>23</sup>,  
T. A. Porter<sup>3</sup>, S. Rainò<sup>13,14</sup>, R. Rando<sup>11,12</sup>, M. Razzano<sup>6</sup>, A. Reimer<sup>50,3</sup>, O. Reimer<sup>50,3</sup>,  
L. C. Reyes<sup>51</sup>, A. Y. Rodriguez<sup>16</sup>, M. Roth<sup>52</sup>, F. Ryde<sup>38,25</sup>, H. F.-W. Sadrozinski<sup>53</sup>,  
R. Sambruna<sup>18</sup>, A. Sander<sup>37</sup>, R. Sato<sup>49,50</sup>, C. Sgrò<sup>6</sup>, M. S. Shaw<sup>3</sup>, E. J. Siskind<sup>55</sup>,  
P. D. Smith<sup>37</sup>, G. Spandre<sup>6</sup>, P. Spinelli<sup>13,14</sup>, L. Stawarz<sup>49,56</sup>, F. W. Stecker<sup>18</sup>,  
M. S. Strickman<sup>1</sup>, D. J. Suson<sup>57</sup>, H. Takahashi<sup>46</sup>, T. Takahashi<sup>49</sup>, T. Tanaka<sup>3</sup>,  
J. B. Thayer<sup>3</sup>, J. G. Thayer<sup>3</sup>, D. J. Thompson<sup>18</sup>, O. Tibolla<sup>58</sup>, D. F. Torres<sup>36,16</sup>, G. Tosti<sup>4,5</sup>,  
A. Tramacere<sup>3,59,60</sup>, Y. Uchiyama<sup>3</sup>, T. L. Usher<sup>3</sup>, V. Vasileiou<sup>19,20</sup>, N. Vilchez<sup>42</sup>,  
M. Villata<sup>61</sup>, V. Vitale<sup>44,62</sup>, A. von Kienlin<sup>48</sup>, A. P. Waite<sup>3</sup>, P. Wang<sup>3</sup>, B. L. Winer<sup>37</sup>,  
K. S. Wood<sup>1</sup>, Z. Yang<sup>24,25</sup>, T. Ylinen<sup>38,63,25</sup>, M. Ziegler<sup>54</sup>, F. Tavecchio<sup>59</sup>, M. Sikora<sup>64</sup>, P.  
Schady<sup>65</sup>, P. Roming<sup>30</sup>, M. M. Chester<sup>30</sup>, L. Maraschi<sup>66</sup>

---

<sup>1</sup>Space Science Division, Naval Research Laboratory, Washington, DC 20375, USA

<sup>2</sup>National Research Council Research Associate, National Academy of Sciences, Washington, DC 20001, USA

<sup>3</sup>W. W. Hansen Experimental Physics Laboratory, Kavli Institute for Particle Astrophysics and Cosmology, Department of Physics and SLAC National Accelerator Laboratory, Stanford University, Stanford, CA 94305, USA

<sup>4</sup>Istituto Nazionale di Fisica Nucleare, Sezione di Perugia, I-06123 Perugia, Italy

<sup>5</sup>Dipartimento di Fisica, Università degli Studi di Perugia, I-06123 Perugia, Italy

<sup>6</sup>Istituto Nazionale di Fisica Nucleare, Sezione di Pisa, I-56127 Pisa, Italy

<sup>7</sup>Laboratoire AIM, CEA-IRFU/CNRS/Université Paris Diderot, Service d’Astrophysique, CEA Saclay, 91191 Gif sur Yvette, France

<sup>8</sup>Istituto Nazionale di Fisica Nucleare, Sezione di Trieste, I-34127 Trieste, Italy

<sup>9</sup>Dipartimento di Fisica, Università di Trieste, I-34127 Trieste, Italy

<sup>10</sup>Rice University, Department of Physics and Astronomy, MS-108, P. O. Box 1892, Houston, TX 77251, USA

<sup>11</sup>Istituto Nazionale di Fisica Nucleare, Sezione di Padova, I-35131 Padova, Italy

<sup>12</sup>Dipartimento di Fisica “G. Galilei”, Università di Padova, I-35131 Padova, Italy

<sup>13</sup>Dipartimento di Fisica “M. Merlin” dell’Università e del Politecnico di Bari, I-70126 Bari, Italy

<sup>14</sup>Istituto Nazionale di Fisica Nucleare, Sezione di Bari, 70126 Bari, Italy

<sup>15</sup>Laboratoire Leprince-Ringuet, École polytechnique, CNRS/IN2P3, Palaiseau, France

<sup>16</sup>Institut de Ciències de l’Espai (IEEC-CSIC), Campus UAB, 08193 Barcelona, Spain

<sup>17</sup>Agenzia Spaziale Italiana (ASI) Science Data Center, I-00044 Frascati (Roma), Italy

<sup>18</sup>NASA Goddard Space Flight Center, Greenbelt, MD 20771, USA

<sup>19</sup>Center for Research and Exploration in Space Science and Technology (CRESST) and NASA Goddard Space Flight Center, Greenbelt, MD 20771, USA

<sup>20</sup>Department of Physics and Center for Space Sciences and Technology, University of Maryland Baltimore County, Baltimore, MD 21250, USA

<sup>21</sup>George Mason University, Fairfax, VA 22030, USA

<sup>22</sup>INAF-Istituto di Astrofisica Spaziale e Fisica Cosmica, I-20133 Milano, Italy

<sup>23</sup>Laboratoire de Physique Théorique et Astroparticules, Université Montpellier 2, CNRS/IN2P3, Montpellier, France

<sup>24</sup>Department of Physics, Stockholm University, AlbaNova, SE-106 91 Stockholm, Sweden

<sup>25</sup>The Oskar Klein Centre for Cosmoparticle Physics, AlbaNova, SE-106 91 Stockholm, Sweden

---

<sup>26</sup>Royal Swedish Academy of Sciences Research Fellow, funded by a grant from the K. A. Wallenberg Foundation

<sup>27</sup>CNRS/IN2P3, Centre d'Études Nucléaires Bordeaux Gradignan, UMR 5797, Gradignan, 33175, France

<sup>28</sup>Université de Bordeaux, Centre d'Études Nucléaires Bordeaux Gradignan, UMR 5797, Gradignan, 33175, France

<sup>29</sup>Dipartimento di Fisica, Università di Udine and Istituto Nazionale di Fisica Nucleare, Sezione di Trieste, Gruppo Collegato di Udine, I-33100 Udine, Italy

<sup>30</sup>Osservatorio Astronomico di Trieste, Istituto Nazionale di Astrofisica, I-34143 Trieste, Italy

<sup>31</sup>Department of Physical Sciences, Hiroshima University, Higashi-Hiroshima, Hiroshima 739-8526, Japan

<sup>32</sup>INAF Istituto di Radioastronomia, 40129 Bologna, Italy

<sup>33</sup>INAF-IASF Bologna, 40129 Bologna, Italy

<sup>34</sup>Max-Planck-Institut für Radioastronomie, Auf dem Hügel 69, 53121 Bonn, Germany

<sup>35</sup>Center for Space Plasma and Aeronomic Research (CSPAR), University of Alabama in Huntsville, Huntsville, AL 35899, USA

<sup>36</sup>Institució Catalana de Recerca i Estudis Avançats (ICREA), Barcelona, Spain

<sup>37</sup>Department of Physics, Center for Cosmology and Astro-Particle Physics, The Ohio State University, Columbus, OH 43210, USA

<sup>38</sup>Department of Physics, Royal Institute of Technology (KTH), AlbaNova, SE-106 91 Stockholm, Sweden

<sup>39</sup>Research Institute for Science and Engineering, Waseda University, 3-4-1, Okubo, Shinjuku, Tokyo, 169-8555 Japan

<sup>40</sup>Department of Physics, Tokyo Institute of Technology, Meguro City, Tokyo 152-8551, Japan

<sup>41</sup>Cosmic Radiation Laboratory, Institute of Physical and Chemical Research (RIKEN), Wako, Saitama 351-0198, Japan

<sup>42</sup>Centre d'Étude Spatiale des Rayonnements, CNRS/UPS, BP 44346, F-30128 Toulouse Cedex 4, France

<sup>43</sup>Department of Physics and Department of Astronomy, University of Maryland, College Park, MD 20742, USA

<sup>44</sup>Istituto Nazionale di Fisica Nucleare, Sezione di Roma “Tor Vergata”, I-00133 Roma, Italy

<sup>45</sup>Department of Physics and Astronomy, University of Denver, Denver, CO 80208, USA

<sup>46</sup>Hiroshima Astrophysical Science Center, Hiroshima University, Higashi-Hiroshima, Hiroshima 739-8526, Japan

<sup>47</sup>Department of Physics, Graduate School of Science, University of Tokyo, 7-3-1 Hongo, Bunkyo-ku, Tokyo 113-0033, Japan

<sup>48</sup>Max-Planck Institut für extraterrestrische Physik, 85748 Garching, Germany

## ABSTRACT

35

36

We present the results from the *Suzaku* X-ray observations of five flat-spectrum radio quasars (FSRQs), namely PKS 0208–512, Q 0827+243, PKS 1127–145, PKS 1510–089 and 3C 454.3. All these sources were additionally monitored simultaneously or quasi-simultaneously by the *Fermi* satellite in gamma-rays and the *Swift* UVOT in the UV and optical bands, respectively. We constructed their broad-band spectra covering the frequency range from  $10^{14}$  Hz up to  $10^{25}$  Hz, and those reveal the nature of high-energy emission of luminous blazars in their low-activity states. The analyzed X-ray spectra are well fitted by a power-law model with photoelectric absorption. In the case of PKS 0208–512, PKS 1127–145, and 3C 454.3, the X-ray continuum showed indication of hard-

---

<sup>49</sup>Institute of Space and Astronautical Science, JAXA, 3-1-1 Yoshinodai, Sagamihara, Kanagawa 229-8510, Japan

<sup>50</sup>Corresponding author, rsato@astro.isas.jaxa.jp

<sup>51</sup>Institut für Astro- und Teilchenphysik and Institut für Theoretische Physik, Leopold-Franzens-Universität Innsbruck, A-6020 Innsbruck, Austria

<sup>52</sup>Kavli Institute for Cosmological Physics, University of Chicago, Chicago, IL 60637, USA

<sup>53</sup>Department of Physics, University of Washington, Seattle, WA 98195-1560, USA

<sup>54</sup>Santa Cruz Institute for Particle Physics, Department of Physics and Department of Astronomy and Astrophysics, University of California at Santa Cruz, Santa Cruz, CA 95064, USA

<sup>55</sup>NYCB Real-Time Computing Inc., Lattingtown, NY 11560-1025, USA

<sup>56</sup>Astronomical Observatory, Jagiellonian University, 30-244 Kraków, Poland

<sup>57</sup>Department of Chemistry and Physics, Purdue University Calumet, Hammond, IN 46323-2094, USA

<sup>58</sup>Institut für Theoretische Physik and Astrophysik, Universität Würzburg, D-97074 Würzburg, Germany

<sup>59</sup>Consorzio Interuniversitario per la Fisica Spaziale (CIFS), I-10133 Torino, Italy

<sup>60</sup>INTEGRAL Science Data Centre, CH-1290 Versoix, Switzerland

<sup>61</sup>INAF, Osservatorio Astronomico di Torino, I-10025 Pino Torinese (TO), Italy

<sup>62</sup>Dipartimento di Fisica, Università di Roma “Tor Vergata”, I-00133 Roma, Italy

<sup>63</sup>School of Pure and Applied Natural Sciences, University of Kalmar, SE-391 82 Kalmar, Sweden

<sup>64</sup>Nicolaus Copernicus Astronomical Center, Bartycka 18, 00-716, Warsaw, Poland

<sup>65</sup>Mullard Space Science Laboratory/UCL, Holmbury St Mary, Dorking, Surrey RH5 6NT

<sup>66</sup>Osservatorio Astronomico di Brena, via Brera, 28, Milano I-20121, Italy

ening at low-energies. Moreover, when compared with the previous X-ray observations, we see a significantly increasing contribution of low-energy photons to the total X-ray fluxes when the sources are getting fainter. The same behavior can be noted in the *Suzaku* data alone. A likely explanation involves a variable, flat-spectrum component produced via inverse-Compton (IC) emission, plus an additional, possibly steady soft X-ray component prominent when the source gets fainter. This soft X-ray excess is represented either by a steep power-law (photon indices  $\Gamma \sim 3 - 5$ ) or a blackbody-type emission with temperatures  $kT \sim 0.1 - 0.2$  keV. We model the broad-band spectra spectra of the five observed FSRQs using synchrotron self-Compton (SSC) and/or external-Compton radiation (ECR) models. Our modeling suggests that the difference between the low- and high-activity states in luminous blazars is due to the different total kinetic power of the jet, most likely related to varying bulk Lorentz factor of the outflow within the blazar emission zone.

*Subject headings:* galaxies: active — quasars: jets — radiation mechanisms: non-thermal – X-rays: galaxies

## 1. Introduction

Observations with the EGRET instrument (30 MeV to 30 GeV; Thompson et al. 1993) on board the Compton Gamma-Ray Observatory (CGRO) have resulted in detection of  $\gamma$ -ray emission from a few hundred astrophysical sources, 66 of which were securely associated with active galactic nuclei (AGNs; e.g., Hartman et al. 1999). Most of the AGNs detected by EGRET show characteristics of the blazar class. Observationally, this class include flat-spectrum radio quasars (FSRQs) and BL Lac objects. FSRQs have strong and broad optical emission lines, while the lines are weak or absent in BL Lacs. During the first three months of the *Fermi* Large Area Telescope’s (LAT) all-sky-survey, 132 bright sources at high Galactic latitudes ( $|b| > 10^\circ$ ) were detected at a confidence level greater than  $10\sigma$  (Abdo et al. 2009a). As expected from the EGRET observations, a large fraction (106) of these sources have been associated with known AGNs (Abdo et al. 2009b). This includes two radio galaxies (Centaurus A and NGC 1275; Abdo et al. 2009c) and 104 blazars consisting of 58 FSRQs, 42 BL Lac objects, and 4 blazars with unknown classification based on their Spectral Energy Distribution (SED).

The radio-to-optical emission of luminous blazars of the FSRQ type is known to be produced by the synchrotron radiation of relativistic electrons accelerated within the outflow, while the inverse Compton (IC) scattering of low-energy photons by the same relativistic

57 electrons is most likely responsible for the formation of the high energy X-ray-to- $\gamma$ -ray com-  
 58 ponent. In addition, it is widely believed that the IC emission from FSRQs is dominated  
 59 by the scattering of soft photons external to the jet (external Compton radiation, ECR).  
 60 These photons, in turn, are produced by the accretion disk, and interact with the jet either  
 61 directly or indirectly, after being scattered or reprocessed in the broad-line region (BLR) or  
 62 a dusty torus (DT; see, e.g., Dermer & Schlickeiser 1993; Sikora et al. 1994; Błażejowski et  
 63 al. 2000). Other sources of seed photons can also contribute to the observed IC radiation,  
 64 and these are in particular jet synchrotron photons through the synchrotron self-Compton  
 65 process (hereafter SSC; Maraschi et al. 1992; Sokolov & Marscher 2005).

66 In this context, detailed X-ray studies offer a unique possibility for discriminating be-  
 67 tween different proposed jet emission models, since those scenarios predict distinct compo-  
 68 nents to be prominent in blazar spectra around keV photon energies. For example, in the  
 69 soft X-ray range a break is expected in the ECR/BLR model, tracking the low-energy end  
 70 of the electron energy distribution (Tavecchio et al. 2000; Sikora et al. 2009). Indeed, both  
 71 the *XMM-Newton* and the *Suzaku* X-ray data of RBS 315 show “convex” spectra (Tavec-  
 72 chio et al. 2007). Such a curvature, on the other hand, can be alternatively accounted for  
 73 by an excess absorption below 1 keV over the Galactic value, or by an intrinsic curvature  
 74 in the electron energy distribution. Furthermore, the situation can be more complex, with  
 75 the simultaneous presence of yet additional components, such as the high-energy tail of the  
 76 synchrotron continuum, SSC emission, or the narrow-band spectral feature originating from  
 77 the “bulk Comptonization” of external UV (disk) radiation by cold electrons within the  
 78 innermost parts of relativistic outflow (Begelman & Sikora 1987; Sikora & Madejski 2000;  
 79 Moderski et al. 2004; Celotti et al. 2007).

80 Ghisellini et al. (1998) have studied the spectral energy distribution of 51 EGRET-  
 81 detected  $\gamma$ -ray loud blazars and have applied the SSC+ECR model to the spectra of these  
 82 sources. Although most of the broadband data collected by Ghisellini et al (1998) cor-  
 83 responded to non-simultaneous measurements, those authors discovered clear trends and  
 84 correlations among the physical quantities obtained from the model calculations. In par-  
 85 ticular, they found an evidence for a well-defined sequence such that the observed spectral  
 86 properties of different blazar classes (BL Lacs and FSRQs) can be explained by an increasing  
 87 contribution of an external radiation field towards cooling jet electrons (thus producing the  
 88 high-energy emission) with the increasing jet power. As a result, while the SSC process alone  
 89 may account for the entire high-energy emission of low-power sources (BL Lacs), a significant  
 90 contribution from the ECR is needed to explain the observed spectra of high-power blazars  
 91 (FSRQs). Meanwhile, when focusing on one particular object, Mukherjee et al. (1999)  
 92 reported that they found a similar trend in the different spectral states of PKS 0528+134.  
 93 They studied the sequence of flaring and low-flux states of the source and found that the

94 SSC mechanism plays a more important role when the source is in a low state, and the ECR  
 95 mechanism is the dominant electron cooling mechanism when the source is in a high  $\gamma$ -ray  
 96 state (see in this context also Sambruna et al. 1997).

97 In order to understand the blazar phenomenon and the differences between BL Lacs and  
 98 FSRQs, as well as the origin of spectral transitions in a particular object, one has to obtain  
 99 truly simultaneous coverage across the entire spectrum, during both flaring and low-activity  
 100 states. However, past  $\gamma$ -ray observations in low-activity states have been limited to only a few  
 101 extremely luminous objects, such as PKS 0528-134 or 3C 279. Only now, with the successful  
 102 launch of the *Fermi* satellite and the excellent performance of the *Suzaku* instruments, do  
 103 we have an opportunity to study high-energy spectra of blazars with substantially improved  
 104 sensitivity, and therefore can probe the different states of the sources’ activity.

105 In this paper, we report the high-sensitivity, broadband *Suzaku* observations of five  
 106 FSRQs, namely PKS 0208–512, Q 0827+243, PKS 1127–145, PKS 1510–089, and 3C 454.3,  
 107 which were bright gamma-ray sources detected by EGRET. Additionally, all of these sources  
 108 were monitored simultaneously or quasi-simultaneously by the *Fermi* LAT and *Swift* Ultravi-  
 109 olet/Optical Telescope (UVOT; Roming et al. 2005). These broadband and high-sensitivity  
 110 observations allow us to reveal the characteristics of the high-energy IC continuum in the  
 111 low-activity states of luminous blazars. The paper is organized as follows: in §2, we describe  
 112 observation and data reduction in the X-ray (*Suzaku*), UV-optical (*Swift* UVOT) and  $\gamma$ -ray  
 113 (*Fermi* LAT) domains. In §3, we present the broad-band analysis results. Finally, in §4  
 114 we discuss the constraints on the jet parameters and speculate on the the origin of differ-  
 115 ent activity states in luminous blazars. Throughout the paper we adopt the cosmological  
 116 parameters  $H_0 = 71 \text{ km s}^{-1} \text{ Mpc}^{-1}$ ,  $\Omega_M = 0.27$ , and  $\Omega_\Lambda = 0.73$ .

## 117 2. Observation and Data Reduction

### 118 2.1. *Suzaku*

119 Five FSRQs were observed by *Suzaku* (Mitsuda et al. 2007) for 40 ks each as one of  
 120 the long-category projects between 2008 October and 2009 January. Table 1 summarizes the  
 121 start time, end time, and the exposures for each observation. *Suzaku* carries four sets of X-ray  
 122 telescopes (Serlemitsos et al. 2007), each with a focal-plane X-ray CCD camera (XIS, X-ray  
 123 Imaging Spectrometer; Koyama et al. 2007) that is sensitive over the 0.3 – 12 keV band,  
 124 together with a non-imaging Hard X-ray Detector (HXD; Takahashi et al. 2007; Kokubun et  
 125 al. 2007), which covers the 10 – 600 keV energy band by utilizing Si PIN photo-diodes and  
 126 GSO scintillation detectors. All of the sources were focused on the nominal center position

127 of the XIS detectors.

128 For the XIS, we used data sets processed using the software of the *Suzaku* data process-  
 129 ing pipeline (ver. 2.2.11.22). Reduction and analysis of the data were performed following  
 130 the standard procedure using the HEADAS v6.5 software package. The screening was based  
 131 on the following criteria: (1) only ASCA-grade 0,2,3,4,6 events were accumulated, while hot  
 132 and flickering pixels were removed using the CLEANSIS script, (2) the time interval after the  
 133 passage of South Atlantic Anomaly was greater than 500 s, and (3) the object was at least  
 134  $5^\circ$  and  $20^\circ$  above the rim of the Earth (ELV) during night and day, respectively. In addition,  
 135 we also selected the data with a cutoff rigidity (COR) larger than 6 GV. The XIS events were  
 136 extracted from a circular region with a radius of  $4.2'$  centered on the source peak, whereas  
 137 the background was accumulated in an annulus with inner and outer radii of  $5.4'$  and  $7.3'$ ,  
 138 respectively. We checked that the use of different source and background regions did not  
 139 affect the analysis results. The response and auxiliary files were produced using the analysis  
 140 tools XISRMFGEN and XISSIMARFGEN developed by the *Suzaku* team, which are included in  
 141 the software package HEASoft version 6.5.

142 The HXD/PIN data (version 2.0) were processed with basically the same screening  
 143 criteria as those for the XIS, except that we required  $\text{ELV} \geq 5^\circ$  through night and day and  
 144  $\text{COR} \geq 8 \text{ GV}$ . The HXD/PIN instrumental background spectra were provided by the HXD  
 145 team for each observation (Kokubun et al. 2007; Fukazawa et al. 2006). Both the source  
 146 and background spectra were made with identical good time intervals and the exposure  
 147 was corrected for detector deadtime of 6.0 – 8.0%. We used the response files, version  
 148 AE\_HXD\_PINHXDNOM5\_20080716.RSP, provided by the HXD team. In our analysis, the  
 149 hard X-ray emission of PKS 1510–089 and 3C454.3 were detected in the energy range from  
 150 12 keV to 40 keV and 50 keV, respectively. For other objects, the sources were not detected  
 151 in the HXD/PIN data. We also note here that all of the objects, the sources were not  
 152 detected in the HXD/GSO data.

Table 1: *Suzaku* observation log of five FSRQs.

Object	$z$	Start time (UT)	Stop time (UT)	XIS/HXD exposures (ks)
0208–512	1.003	2008 Dec 14 07:33	2008 Dec 15 11:30	50.3/39.3
0827+243	0.939	2008 Oct 27 05:11	2008 Oct 28 08:04	35.3/36.3
1127–145	1.187	2008 Nov 29 18:10	2008 Nov 30 22:51	42.2/29.0
1510–089	0.361	2009 Jan 27 04:32	2009 Jan 28 05:25	38.5/36.2
3C454.3	0.859	2008 Nov 22 09:19	2008 Nov 23 16:31	39.9/40.4

## 2.2. *Swift*

153

154 Four analyzed FSRQs (PKS 0208–512, Q 0827+243, PKS 1510–089, and 3C 454.3) were  
 155 observed with *Swift* between 2008 October and 2009 January, as part of *Swift* “target of  
 156 opportunity” observations. We analyzed the data taken within or near the time of the  
 157 *Suzaku* observations. For the case of PKS 1127–145, however, the observations were made  
 158 only once in 2007 March. We focused on analysis of the UVOT data, since *Suzaku* provides  
 159 much better photon statistics in X-rays than *Swift* X-ray Telescope (XRT; Burrows et al.  
 160 2005) and Burst Alert Telescope (BAT; Barthelmy et al. 2005), thanks to the long *Suzaku*  
 161 exposures. We used the XRT data primarily for a consistency check regarding the spectral  
 162 properties. Table 2 summarizes the start time, exposure time, and filters used for each  
 163 observation.

164 The UVOT observing mode commonly takes an exposure in each of the six optical and  
 165 ultraviolet filters (*v*, *b*, *u*, uvw1, uvm2, and uvw2) per *Swift* pointing. The list of UVOT  
 166 observations is given in Table 2. For the screening, reduction and analysis of the *Swift* data,  
 167 we used standard procedures within the HEASoft v.6.5 software package with the calibration  
 168 database updated as of 2009 February 28. For this analysis, Level 2 sky-corrected image data  
 169 were used. Since all sources were relatively bright, the source aperture sizes were chosen to  
 170 correspond to those used to determine the UVOT zero points: 5'' for the optical and UV  
 171 filters (Poole et al. 2008). The background was extracted from a nearby source-free circular  
 172 region with 15'' radius. All image data were corrected for coincidence loss. The observed  
 173 magnitudes were converted into flux densities by the standard procedures (Poole et al. 2008).

174 The XRT data were all taken in Photon Counting mode (PC mode; Hill et al. 2004). The  
 175 data were reduced by the XRT data analysis task XRTPIPELINE version 0.12.0. Photons were  
 176 selected from the event file by xselect version 2.4. The auxiliary response file was created by  
 177 the XRT task XRTMKARF and the standard response file SWXPC0TO12S6\_20010101V011.RMF.  
 178 All spectra were analyzed in the 0.3–10.0 keV band using XSPEC version 11.3.2.

179

## 2.3. *Fermi* LAT

180 During the first year of *Fermi* Large Area Telescope (LAT; Atwood et al. 2009) oper-  
 181 ation, most of the telescope’s time has been dedicated to “survey mode” observing, where  
 182 *Fermi* points away from the Earth, and nominally rocks the spacecraft axis north and south  
 183 from the orbital plane to enable monitoring of the entire sky every  $\sim 3$  hours (or 2 orbits).  
 184 We analyzed the LAT’s observations of the five blazar regions using data collected during  
 185 the first 4-5 months centered around *Suzaku* observations. Little variability indicated by the

Table 2: *Swift* observation log of five FSRQs.

Object	obsID	Start time (UT)	Exposure <sup>a</sup> (ks)	Exposure <sup>b</sup> (ks)	Filter <sup>b</sup>
0208–512	00035002024	2008 Dec 14 15:25	0.99	0.94	all
0827+243	00036375004	2008 Dec 08 13:42	1.72	1.71	<i>u</i>
1127–145	00036380001	2007 Mar 24 00:32	14.6	14.2	all
1510–089	00031173010	2009 Jan 25 18:40	3.46	3.40	<i>u</i> , w1, m2
3C 454.3	00035030030	2008 Oct 26 20:28	0.43	0.40	all

<sup>a</sup>*Swift* XRT

<sup>b</sup>*Swift* UVOT

186 LAT lightcurves for the studied objects during this time implies that the constructed broad-  
 187 band spectra, even though not exactly simultaneous, are representative for the low-activity  
 188 states of all five blazars.

189 The data used here comprise all scientific data obtained between 4 August and 19  
 190 December 2008 for PKS 0208–512, Q 0827+243, PKS 1127–145 and 3C 454.3 (interval runs  
 191 from Mission Elapsed Time (MET) 239557417 to 251345942), and 4 August 2008 and 30  
 192 January 2009 for 1510–089 (MET 239557417 to 254966035), respectively . We have applied  
 193 the zenith angle cut to eliminate photons from the Earth’s limb, at 105°. This is important  
 194 in pointed mode observations, but also important for survey mode due to overshoots and sun  
 195 avoidance maneuvers. In addition, we excluded the time intervals when the rocking angle  
 196 was more than 43°. We use the “Diffuse” class events (Atwood et al. 2009), which, of all  
 197 reconstructed events have the highest probability of being photons.

198 In the analysis presented here, we set the lower energy bound to a value of 200 MeV,  
 199 since the bin counts for photons with energies of  $\sim 100$  MeV and lower are systematically  
 200 lower than expected based on extrapolations of a reasonable functions. Science Tools version  
 201 v9r14 and IRFs (Instrumental Response Functions) P6\_V3 were used.

202 **3. Results**

203 **3.1. Suzaku**

204 *3.1.1. Temporal analysis*

205 Figure 1 shows the count rate variations of the five observed FSRQs. The summed XISs  
 206 (XIS0,1,3) light curves are shown separately in different energy bands: 0.5–2 keV (*upper*  
 207 panel), 2–10 keV (*middle* panel), and 0.5–10 keV (*bottom* panel), respectively. Since the  
 208 count rate variations of the HXD/PIN detector were less clear due to limited photon statistics  
 209 and uncertainty of the modeling of the non-X-ray background, we only concentrate on the  
 210 temporal variability of the XIS data below 10 keV. We evaluate the fractional variability by  
 211 calculating the variability amplitude relative to the mean count rate corrected for effects  
 212 of random errors (e.g., Edelson et al. 2002):  $F_{\text{var}} = \sqrt{S^2 - \overline{\sigma_{\text{err}}^2}}/\bar{x}$ , where  $S^2$  is the total  
 213 variance of the light curve,  $\overline{\sigma_{\text{err}}^2}$  is the mean error squared and  $\bar{x}$  is the mean count rate.  
 214 The variability amplitude in the XIS bands are  $F_{\text{var}} = 0.036 \pm 0.021$  for 0208–512,  $F_{\text{var}} =$   
 215  $0.027 \pm 0.010$  for 1127–145, and  $F_{\text{var}} = 0.025 \pm 0.008$  for 1510–089, respectively. 0827+243  
 216 and 3C454.3 show only weak variability, which is not significant.

217 *3.1.2. Time-averaged spectral analysis*

218 In the following we report the analysis procedure and results for each object. The  
 219 background-subtracted spectra were fitted using XSPEC ver.11.3.2. All errors are quoted at  
 220 the 90% confidence level for the parameter of interest unless otherwise stated. All the fits in  
 221 this paper are restricted to the energy ranges of 0.5–10 keV (XIS0,3: the FI chips), 0.3–8 keV  
 222 (XIS1: the BI chip), 12–40 keV for PKS 1510–089, and 12–50 keV for 3C 454.3 (HXD/PIN).  
 223 We fixed the relative normalization of the XISs and HXD/PIN at 1.13, which is carefully  
 224 determined from the XIS calibration using nominal pointings of the Crab Nebula. Serlemitsos  
 225 et al. (2007) reported that spectral normalizations are slightly different (a few percent)  
 226 among the CCD sensors based on a contemporaneous fit of the Crab spectra. Therefore,  
 227 we adjusted the normalization factor among the three XISs relative to XIS0. The results of  
 228 the spectral fits with a simple absorbed power-law model are summarized in Table 3 (with  
 229 Galactic absorption) and Table 4.

Table 3: Results of the spectral fits to the *Suzaku* data using a power-law with Galactic absorption

Object	$N_{\text{H}}^{\text{a}}$	$\Gamma$	$F_{2-10\text{keV}}^{\text{b}}$	constant (XIS0,1,3,HXD/PIN)	$\chi_{\text{r}}^2$ (dof)
0208–512	3.08 (fixed)	$1.68 \pm 0.03$	$1.37 \pm 0.06$	$1, 1.04 \pm 0.05, 1.04 \pm 0.05, \text{None}$	0.91 (250)
0827+243	3.62 (fixed)	$1.46 \pm 0.04$	$1.37 \pm 0.07$	$1, 0.90 \pm 0.05, 1.04 \pm 0.06, \text{None}$	0.84 (194)
1127–145	3.83 (fixed)	$1.41 \pm 0.02$	$3.45 \pm 0.08$	$1, 1.03 \pm 0.03, 1.05 \pm 0.03, \text{None}$	1.01 (331)
1510–089	7.88 (fixed)	$1.37 \pm 0.01$	$6.31 \pm 0.12$	$1, 1.00 \pm 0.02, 1.02 \pm 0.02, 1.13$	1.06 (407)
3C 454.3	7.24 (fixed)	$1.58 \pm 0.01$	$16.7 \pm 0.2$	$1, 1.04 \pm 0.01, 1.02 \pm 0.01, 1.13$	1.00 (1090)

Errors correspond to 90% confidence level.

<sup>a</sup>Fixed value indicates the Galactic absorption column density in units of  $10^{20} \text{ cm}^{-2}$ .

<sup>b</sup>Flux in units of  $10^{-12} \text{ erg cm}^{-2} \text{ s}^{-1}$ .

### PKS 0208–512

230

231 The time averaged, background subtracted three XIS spectra of PKS 0208–512, when fitted  
 232 jointly, are well described by a single absorbed power-law model, and the absorption column  
 233 is consistent with the Galactic value  $N_{\text{H}} = 3.08 \times 10^{20} \text{ cm}^{-2}$  (Dickey & Lockman 1990).  
 234 We obtained the best fit photon index  $\Gamma = 1.68 \pm 0.02$  and the 2 – 10 keV flux  $F_{2-10\text{keV}} =$   
 235  $(1.37 \pm 0.03) \times 10^{-12} \text{ erg cm}^{-2} \text{ s}^{-1}$  with a chi-squared value of 0.91 for 250 dof. Figure 2  
 236 shows the spectra obtained with the XISs with residuals plotted against the best-fit power-  
 237 law model with Galactic absorption. Although statistically acceptable, we notice that the  
 238 residuals of the fits show moderate excess feature at low energies, below 1 keV.

239 In the previous observation with BeppoSAX during a high flux state (Tavecchio et  
 240 al. 2002),  $F_{2-10\text{keV}} \sim 4.7 \times 10^{-12} \text{ erg cm}^{-2} \text{ s}^{-1}$  - which is a factor of three larger than in our  
 241 *Suzaku* observations - the X-ray spectrum is well described by a power-law with photon index  
 242  $\Gamma \sim 1.7$ , similar to the *Suzaku* result. However, Tavecchio et al. reported that the spectrum  
 243 was heavily absorbed below 1 keV, indicating a column density of  $N_{\text{H}} = 1.67 \times 10^{21} \text{ cm}^{-2}$ .  
 244 Figure 4 shows the *Suzaku* spectrum with residuals assuming such an increased value of  $N_{\text{H}}$ .  
 245 The residuals indicate significant soft excess emission below 1 keV, if  $N_{\text{H}}$  is the same as found  
 246 in the previous BeppoSAX observation.

247 The variable soft X-ray emission of PKS 0208–512 may indicate that the convex spec-  
 248 trum observed by BeppoSAX reflects an intrinsic IC continuum shape, while the soft excess  
 249 observed by *Suzaku* reflects the presence of an additional spectral component which becomes  
 250 prominent when the source gets fainter (see Tavecchio et al. 2007; Kataoka et al. 2008).

Table 4: Results of the spectral fits to the *Suzaku* data with best fit models

Object	Model <sup>a</sup>	$N_{\text{H}}$	$\Gamma_{\text{hi}}$ <sup>b</sup>	$\Gamma_{\text{low}}$ <sup>c</sup>	$F_{2-10\text{keV}}$ <sup>d</sup>	kT (keV)	$\chi_r^2$
0208–512	PL	3.08 (fixed)	$1.68 \pm 0.03$	-	$1.37 \pm 0.06$	-	0.91 (250)
0827+243	PL	3.62 (fixed)	$1.46 \pm 0.04$	-	$1.37 \pm 0.07$	-	0.84 (194)
1127–145	PL	$10.8^{+1.6}_{-1.5}$	$1.52 \pm 0.03$	-	$3.36 \pm 0.08$	-	0.82 (330)
1510–089	PL+BB	7.88 (fixed)	$1.32 \pm 0.03$	-	$6.42 \pm 0.13$	$0.15 \pm 0.03$	0.97 (405)
	PL+PL	7.88 (fixed)	$1.26^{+0.06}_{-0.12}$	$2.85^{+0.88}_{-0.40}$	$6.30^{+0.18}_{-0.74}$	-	0.96 (405)
3C 454.3	PL	$9.07^{+0.58}_{-0.57}$	$1.62 \pm 0.01$	-	$16.6 \pm 0.2$	-	0.97 (1089)

<sup>a</sup>Spectral fitting models. PL, power-law function; PL+PL, double power-law function; PL+BB, power-law + blackbody model.

<sup>b</sup>Differential spectral photon index.

<sup>c</sup>Differential spectral photon index at the low-energy X-ray band, when fitted with a double power-law function.

<sup>d</sup>Flux in units of  $10^{-12} \text{ erg cm}^{-2} \text{ s}^{-1}$ .

251 Therefore, to model in more detail the observed X-ray spectrum, we first considered a double  
 252 power-law fit (PL + PL) in which the soft X-ray excess is represented by a steep power-law  
 253 component. The absorption column is fixed at  $N_{\text{H}} = 1.67 \times 10^{21} \text{ cm}^{-2}$ , as given by Tavecchio  
 254 et al. (2002). We obtained the photon indices  $\Gamma_1 = 4.98 \pm 0.30$  and  $\Gamma_2 = 1.71^{+0.02}_{-0.04}$ . This  
 255 provides an acceptable fit, with  $\chi_r^2/\text{dof} = 0.90/248$ . We also considered an alternative fit  
 256 consisting of a power-law function and a blackbody component. This model also gives a  
 257 similarly good representation of the data with  $\chi_r^2/\text{dof} = 0.90/248$ , implying  $\Gamma = 1.78 \pm 0.03$   
 258 and the temperature of the introduced thermal component of  $kT = 0.092 \pm 0.003 \text{ keV}$ . Both  
 259 fits appear to be as good as a single power-law with free absorption, and do not improve the  
 260 goodness of fit.

### 261 *Q 0827+243*

262 The time averaged spectra of Q 0827+243 collected with the XISs are well fitted by an  
 263 absorbed power-law model with a photon index  $\Gamma = 1.46 \pm 0.02$  ( $\chi_r^2 = 0.84$  for 194 dof). The  
 264 absorption column is consistent with the Galactic value of  $N_{\text{H}} = 3.62 \times 10^{20} \text{ cm}^{-2}$  (Dickey &  
 265 Lockman 1990), and the flux over 2 – 10 keV is  $F_{2-10\text{keV}} = (1.37 \pm 0.04) \times 10^{-12} \text{ erg cm}^{-2} \text{ s}^{-1}$ .  
 266 As shown in Figure 2, there is no evidence for any additional spectral feature in the soft band.  
 267 This result is in good agreement with previous *Chandra* observations of the core (Jorstad &  
 268 Marscher 2004), revealing that the X-ray continuum is well described by a power-law model

269 ( $\Gamma \sim 1.4$ ) with Galactic absorption.

270

*PKS 1127–145*

271 We first fitted the XISs spectra with a single power-law model with a Galactic absorption of  
 272  $N_{\text{H}} = 3.83 \times 10^{20} \text{ cm}^{-2}$  (Murphy et al. 1996). We obtained the photon index of  $\Gamma = 1.41 \pm 0.01$   
 273  $\chi_{\text{r}}^2 = 1.01$  for 331 dof), but the residuals show a substantial deficit of photons at low energies  
 274 (Figure 2). To investigate this deficit in more detail, we fitted the spectra with a single  
 275 power-law and a free absorption model. This model represents well the spectra with the best  
 276 chi-squared value of 0.82 for 330 dof (Figure 3), indicating that the column density is higher  
 277 than the Galactic value at the 99.9% confidence level. For this model the photon index is  
 278  $\Gamma = 1.51 \pm 0.02$  and the unabsorbed X-ray flux is  $F_{2-10\text{keV}} = (3.36 \pm 0.05) \times 10^{-12} \text{ erg cm}^{-2} \text{ s}^{-1}$ .  
 279 The best-fit column density is  $N_{\text{H}} = (1.08 \pm 0.09) \times 10^{21} \text{ cm}^{-2}$ , which is similar to the one  
 280 found in previous *Chandra* and *XMM-Newton* observations ( $N_{\text{H}} \sim 1.2 \times 10^{21} \text{ cm}^{-2}$ ) during a  
 281 high state with  $F_{2-10\text{keV}} \sim 6 \times 10^{-12} \text{ erg cm}^{-2} \text{ s}^{-1}$  (Bechtold et al. 2001; Foschini et al. 2006).  
 282 We note that the Galactic absorption and a broken power-law model also well represents the  
 283 spectra with  $\chi_{\text{r}}^2/\text{dof}$  of 0.81/329. In this model, the spectrum below  $E_{\text{brk}} = 1.50 \pm 0.08 \text{ keV}$   
 284 is rather hard ( $\Gamma_1 = 1.10 \pm 0.05$ ), and the high energy photon index is  $\Gamma_2 = 1.50 \pm 0.02$ .

285

*PKS 1510–089*

286 Figure 2 shows the XISs and HXD/PIN spectra of PKS 1510–089 (including residuals), plot-  
 287 ted against the best-fit power-law model with Galactic absorption, using the overall X-ray  
 288 data between 0.3 and 40 keV. The best fit photon index is  $\Gamma = 1.37 \pm 0.01$  and the unab-  
 289 sorbed X-ray flux is  $F_{2-10\text{keV}} = (6.31 \pm 0.07) \times 10^{-12} \text{ erg cm}^{-2} \text{ s}^{-1}$ . However, this model did  
 290 not represent the spectra well yielding a chi-squared value of 1.06 for 407 dof. The residuals  
 291 indicate some excess emission at low energies.

292 To represent the observed X-ray spectra, we tried the same analysis as for PKS 0208–512.  
 293 We first fitted the data by a double power-law model with Galactic absorption. We obtained  
 294 the photon indices  $\Gamma_1 = 2.84_{-0.47}^{+0.50}$  and  $\Gamma_2 = 1.26_{-0.06}^{+0.04}$ . This provides an acceptable fit, with  
 295  $\chi_{\text{r}}^2/\text{dof} = 0.96/405$ . The improvement of the chi-squared statistic is significant at more than  
 296 the 99.9% confidence level when compared to the single power-law model. Next, we consid-  
 297 ered an alternative fit consisting of a power-law function and a blackbody component. This  
 298 model also gives a good representation of the data, with  $\chi_{\text{r}}^2$  of 0.97 for 405 dof, indicating that  
 299 the photon index is  $\Gamma = 1.32 \pm 0.02$  and the temperature of the introduced thermal compo-  
 300 nent is  $kT = 0.15 \pm 0.02 \text{ keV}$ . This result is consistent with previous *Suzaku* ( $\Gamma = 1.24 \pm 0.01$ ;  
 301 Kataoka et al. 2008) and BeppoSAX observations ( $\Gamma = 1.39 \pm 0.08$ ; Tavecchio et al. 2000).

3C 454.3

302

303 We first fitted the XISs and PIN spectra with a single power-law model with a Galactic  
 304 absorption of  $N_{\text{H}} = 7.24 \times 10^{20} \text{ cm}^{-2}$  (Murphy et al. 1996). We obtained the photon index of  
 305  $\Gamma = 1.41 \pm 0.01$  ( $\chi_{\text{r}}^2 = 1.00$  for 1090 dof), but the residuals show some scatter around 1 keV.  
 306 To investigate this scatter in more detail, we fitted the spectra with a single power-law and  
 307 a free absorption model. This model represents well the spectra with the best chi-squared  
 308 value of 0.97 for 1089 dof, indicating that the column density is higher than the Galactic  
 309 value at the 99.9% confidence level. For this model the photon index is  $\Gamma = 1.51 \pm 0.02$  and  
 310 the unabsorbed X-ray flux is  $F_{2-10\text{keV}} = (3.36 \pm 0.05) \times 10^{-12} \text{ erg cm}^{-2} \text{ s}^{-1}$ .

311 In the case of 3C 454.3 we obtained the best fit to the XISs and HXD/PIN spectra  
 312 assuming an absorbed power-law model with a photon index of  $\Gamma = 1.61 \pm 0.01$  and a  
 313 column density of  $N_{\text{H}} = (9.07 \pm 0.35) \times 10^{20} \text{ cm}^{-2}$ , which is larger than the Galactic value  
 314 at the 99.9% confidence level. The unabsorbed 2 – 10 keV flux is  $F_{2-10\text{keV}} = (1.66 \pm 0.01) \times$   
 315  $10^{-11} \text{ erg cm}^{-2} \text{ s}^{-1}$  (Figure 2). The spectra can be fitted with both the Galactic absorption  
 316 and a broken power-law model as well as the above model ( $\chi_{\text{r}}^2/\text{dof}$  of 0.96/1088). In the  
 317 former case, the photon indices are  $\Gamma_1 = 1.47_{-0.03}^{+0.01}$  and  $\Gamma_2 = 1.61 \pm 0.01$ , while the break  
 318 energy is  $E_{\text{brk}} = 1.29_{-0.11}^{+0.08} \text{ keV}$ . In addition, we reanalyzed the previous *Suzaku* data collected  
 319 in December 2007 during the high state (Donnarumma et al. 2010). The time averaged  
 320 XISs and HXD/PIN spectra was well described by a single absorbed power-law model with  
 321  $\Gamma = 1.64 \pm 0.01$ , implying the flux  $F_{2-10\text{keV}} = (3.09 \pm 0.02) \times 10^{-11} \text{ erg cm}^{-2} \text{ s}^{-1}$ , which is  
 322 larger by a factor of two than the one found in our 2008 observations. The absorption column  
 323 also shows a higher value of  $N_{\text{H}} = (1.07 \pm 0.03) \times 10^{21} \text{ cm}^{-2}$ .

324 Figure 5 shows the unfolded spectra obtained in 2007 (high state) and 2008 (this work;  
 325 low state). The bottom panel shows the residuals by subtracting the spectra in the high  
 326 state from those in the low state. The excess emission at low energies is clearly visible in  
 327 the residuals.

328 The previous X-ray observations of 3C 454.3 often indicated some additional absorption  
 329 in excess to the Galactic value. For example, Villata et al. (2006) reported  $N_{\text{H}} = (1.34 \pm$   
 330  $0.05) \times 10^{21} \text{ cm}^{-2}$  in the *Chandra* data collected in May 2005, during the outburst phase  
 331 ( $F_{2-8\text{keV}} \sim 8.4 \times 10^{-11} \text{ erg cm}^{-2} \text{ s}^{-1}$ , which is  $\sim 5$  times higher than in our observation). An  
 332 even higher hydrogen column density was found by Giommi et al. (2006), when fitting the  
 333 April-May 2005 data taken by the *Swift* XRT ( $N_{\text{H}} \sim 2 - 3 \times 10^{21} \text{ cm}^{-2}$ ), and by Atari et al.  
 334 (2007, 2008), using the July and December 2006, and May 2007 data taken by XMM-*Newton*.  
 335 Assuming that the intrinsic absorption in 3C 454.3 is the same as reported in Villata et al.  
 336 (2006), we fit our *Suzaku* data first by a double power-law function, obtaining  $\Gamma_1 = 3.66_{-0.33}^{+0.35}$   
 337 and  $\Gamma_2 = 1.61 \pm 0.02$ . This provides an acceptable fit, with  $\chi_{\text{r}}^2/\text{dof} = 0.97/1088$ . Next

338 we consider an alternative fit consisting of a power-law and a blackbody component. This  
 339 model gives a good representation of the data, with  $\chi_r^2/\text{dof} = 1.00/1088$ , a photon index  
 340 of  $\Gamma = 1.65 \pm 0.01$ , and a temperature of  $kT = 0.105 \pm 0.004$  keV. However, the fitting  
 341 results do not improve the goodness of fit compared with the single power-law model with  
 342 free absorption.

### 3.1.3. Time-resolved spectral analysis

344 In order to investigate the X-ray spectral evolution of each object, we divided the total  
 345 exposure into one-orbit intervals ( $\sim 5760$  s). We fitted the overall XIS spectra between 0.3  
 346 and 10 keV with an absorbed simple power-law function. The photoelectric absorbing column  
 347 densities were fixed at the values derived in §3.1.2. Figure 6 shows the relation between  
 348 the 2 – 10 keV fluxes versus the photon indices measured by the *Suzaku* XISs. Significant  
 349 spectral variation is seen in PKS 0208–512 ( $\Gamma = 1.4 - 1.8$ ), Q 0827+243 ( $\Gamma = 1.2 - 1.6$ ),  
 350 PKS 1127–145 ( $\Gamma = 1.4 - 1.6$ ), and PKS 1510–089 ( $\Gamma = 1.3 - 1.5$ ). In the case of 3C 454.3,  
 351 the X-ray photon index is only weakly variable around the mean value  $\Gamma \sim 1.6$ . Figure 6  
 352 clearly reveals a spectral evolution with the X-ray spectra hardening as the sources become  
 353 brighter. Such a trend is often observed in high-frequency-peaked BL Lac objects (e.g.,  
 354 Kataoka et al. 1999), but it has never been observed so clearly in FSRQs (but see Kataoka  
 355 et al. 2008 for PKS 1510–089).

## 3.2. *Swift*

356  
 357 Since the effective area of the *Swift* XRT is less than 10% of the *Suzaku* XIS in the  
 358 0.5–10 keV range, detailed spectral modeling is difficult using *Swift* data. Furthermore, the  
 359 average exposure for the *Swift* observation was only a few kiloseconds, which was much less  
 360 than the *Suzaku* exposure. We therefore fit the XRT data simply with a power-law model  
 361 with Galactic absorption in the energy range 0.3–10 keV for the cross-calibration between  
 362 the two instruments. The results of the spectral fits are summarized in Table 5. We can see  
 363 that the results obtained with *Suzaku* and *Swift* are consistent within the range of error  
 364 except PKS 1127–145.

365 The UVOT fluxes in each filter were corrected for Galactic extinction following the  
 366 procedure described in Cardelli et al. (1989). We generated a list of the amount of extinc-  
 367 tion that needs to be accounted for in each filter,  $A_\lambda = E_{B-V}(aR_V + b)$ , where  $a$  and  $b$   
 368 are constants. The Cardelli procedure provides a good approximation to the UV-through-

Table 5: Results of the spectral fits to the *Swift* XRT data using a power-law with Galactic absorption

Object	$N_{\text{H}}^{\text{a}}$	$\Gamma$	$F_{2-10\text{keV}}^{\text{b}}$	$\chi_{\text{r}}^2$ (dof)
0208–512	3.08 (fixed)	$1.96 \pm 0.24$	$1.37 \pm 0.06$	0.33 (13)
0827+243	3.62 (fixed)	$1.46 \pm 0.35$	$1.13_{-0.43}^{+0.55}$	1.12 (8)
1127–145	3.83 (fixed)	$1.28 \pm 0.03$	$6.14 \pm 0.23$	1.28 (94)
1510–089	7.88 (fixed)	$1.38 \pm 0.08$	$6.09_{-0.62}^{+0.65}$	0.71 (31)
3C 454.3	7.24 (fixed)	$1.53 \pm 0.09$	$17.6 \pm 2.1$	1.41 (18)

Errors correspond to  $1\sigma$  confidence level.

<sup>a</sup>Fixed value indicates the Galactic absorption column density in units of  $10^{20} \text{ cm}^{-2}$ .

<sup>b</sup>Flux in units of  $10^{-12} \text{ erg cm}^{-2} \text{ s}^{-1}$ .

369 IR Galactic dust extinction as a function of the total-to-selective extinction,  $R_V$ , which  
 370 throughout this paper we assume to be  $R_V = 3.1$ , which is the mean Galactic value. The  
 371 observed magnitudes and correction factors for each of the filters are summarized in Table 6  
 and Table 7, respectively.

Table 6: *Swift* UVOT magnitudes of five FSRQs

Object	$v$ (mag)	$b$ (mag)	$u$ (mag)	uvw1 (mag)	uvm2 (mag)	uvw2 (mag)	E(B-V)
0208–512	$17.64_{-0.12}^{+0.14}$	$17.94_{-0.08}^{+0.09}$	$17.17_{-0.08}^{+0.09}$	$16.84 \pm 0.07$	$16.71 \pm 0.07$	$17.00_{-0.05}^{+0.06}$	0.022
0827+243	-	-	$16.57 \pm 0.01$	-	-	-	0.033
1127–145	$16.48 \pm 0.02$	$16.70 \pm 0.01$	$15.64 \pm 0.01$	$15.51 \pm 0.01$	$15.56 \pm 0.01$	$15.79 \pm 0.01$	0.037
1510–089	-	-	$16.01 \pm 0.02$	$16.27 \pm 0.02$	$16.13 \pm 0.02$	-	0.097
3C 454.3	$16.05_{-0.08}^{+0.09}$	$16.52 \pm 0.06$	$15.72 \pm 0.06$	$15.75 \pm 0.06$	$15.81 \pm 0.08$	$16.06 \pm 0.05$	0.107

Observed magnitude for each observation using specific filter (Galactic extinction not corrected).

372

373

### 3.3. *Fermi* LAT

374

375

To study the average spectra of five objects during the four or five months of observations, we use the standard maximum-likelihood spectral estimator provided with the LAT

Table 7: Correction factors for the Galactic extinction in UV and optical filters

Param		$v$	$b$	$u$	uvw1	uvm2	uvw2
$\lambda^a$	(nm)	547	439	346	260	249	193
$a^b$		1.0015	0.9994	0.9226	0.4346	0.3494	-0.0581
$b^b$		0.0126	1.0171	2.1019	5.3286	6.1427	8.4402
	0208–512	0.07	0.09	0.11	0.15	0.16	0.18
	0827+243	-	-	0.16	-	-	-
$A_\lambda^b$	1127–145	0.12	0.15	0.18	0.25	0.27	0.31
	1510–089	-	-	0.48	0.65	0.70	-
	3C 454.3	0.33	0.44	0.53	0.71	0.77	0.88

<sup>a</sup>Center wavelength for each optical and UV filter.

<sup>b</sup>Parameters for calculating Galactic extinction for optical and UV filters, calculated according to the prescription in Cardelli et al. (1989). The Galactic reddening was taken from Schlegel et al. (1998).

376 science tools GTLIKE. This fits the data to a source model, along with models for the uniform  
 377 extragalactic and structured Galactic backgrounds. Photons were extracted from a region  
 378 with a  $10^\circ$  radius centered on the coordinates of the position of each object. The Galactic  
 379 diffuse background model is the currently recommended version (glliem\_v02 <sup>1</sup>), with the  
 380 normalization free to vary in the fit. The response function used is P6\_V3\_DIFFUSE.

381 For simplicity, we model the continuum emission from each source with a single power-  
 382 law. It is likely that such a model might be too simple, as shown in the paper reporting  
 383 spectra of bright Fermi blazars (Abdo et al. 2010), where the gamma-ray data suggest a  
 384 steepening of the spectrum with energy, well-described as a broken power-law. However, here,  
 385 we are reporting cases of blazars in low-level activity states and thus relatively faint, where  
 386 fits to a broken power-law model would result in poorly constrained spectral parameters for a  
 387 more complex model; furthermore, we note that the use of such more complex spectral model  
 388 in the gamma-ray band does not alter our conclusions or significantly change the parameters  
 389 in Table 10. The extragalactic background is assumed to have a power-law spectrum, with  
 390 its spectral index and the normalization free to vary in the fit. From an unbinned GTLIKE  
 391 fit the best fit photon indices are  $\Gamma = 2.33 \pm 0.05$  for PKS 0208–512,  $\Gamma = 2.62 \pm 0.35$  for  
 392 Q 0827+243,  $\Gamma = 2.77 \pm 0.14$  for PKS 1127–145,  $\Gamma = 2.48 \pm 0.03$  for PKS 1510–089, and  
 393  $\Gamma = 2.51 \pm 0.02$  for 3C 454.3 (see also Table 8). Here only statistical errors are taken into

<sup>1</sup>This model is available for download from the Fermi Science Support Center, <http://fermi.gsfc.nasa.gov/ssc>.

394 account, and we report fluxes using spectra extrapolated down to 100 MeV. In the case of  
 395 bright sources (PKS 1510–089 and 3C 454.3), we also analyzed the data collected during the  
 396 *Suzaku* observing period to construct the simultaneous broad-band spectra spectra.

397 Table 9 summarizes the flux in seven energy bands obtained by separately running  
 398 GTLIKE for each energy band; 200–400 keV, 400–800 keV, 800–1600 keV, 1600–3200 keV,  
 399 3200–6400 keV, 6400–12800 keV, 12800–25600 keV, respectively.

Table 8: Results of the spectral fits to the *Fermi* LAT data

Object	$\Gamma$	$F_{>100\text{MeV}}^{\text{a}}$	TS <sup>b</sup>
0208–512	2.33±0.05	0.26±0.03	1484
0827+243	2.62±0.36	0.05±0.04	58
1127–145	2.75±0.14	0.15±0.04	234
1510–089	2.48±0.03	0.69±0.04	4224
3C 454.3	2.50±0.02	2.55±0.08	25144
1510–089 <sup>c</sup>	2.28±0.27	0.91±0.51	59
3C 454.3 <sup>c</sup>	2.62±0.13	2.59±0.58	281

<sup>a</sup>Flux in units of  $10^{-6}$  ph cm<sup>-2</sup> s<sup>-1</sup>.

<sup>b</sup>Test statistic: defined as  $\text{TS} = 2(\log L - \log L_0)$ , where  $L$  and  $L_0$  are the likelihood when the source is included or not.

<sup>c</sup>Corresponding data collected during the *Suzaku* observing period.

## 400 4. Discussion

### 401 4.1. Broad-Band Spectra spectral fits

402 We constructed the broad-band spectral energy distribution (SED) ranging from the  
 403 radio to  $\gamma$ -ray bands for the five observed FSRQs, and these are shown in Figure 7. Here  
 404 the filled red circles and solid lines represent simultaneous data from the UV/optical (*Swift*  
 405 UVOT), X-ray (*Suzaku*) and  $\gamma$ -ray (*Fermi* LAT) observations. Quasi-simultaneous data  
 406 are also shown as red open triangles and dashed lines. Historical radio (NED) and  $\gamma$ -  
 407 ray (EGRET) data are also plotted as filled blue circles. Green symbols in the SEDs of  
 408 PKS 1510–089 and 3C 454.3 denote the previous simultaneous observations (Kataoka et al.  
 409 2008; Donnarumma et al. 2010).

410 In order to model the constructed SEDs, we applied the synchrotron-inverse Compton

Table 9: Results of *Fermi* LAT data analysis from 200 MeV to 25600 MeV (Flux in units of  $10^{-9}$  ph MeV $^{-1}$  cm $^{-2}$  s $^{-1}$ )

Object	Band 1 <sup>a</sup>	Band 2 <sup>a</sup>	Band 3 <sup>a</sup>	Band 4 <sup>a</sup>	Band 5 <sup>a</sup>	Band 6 <sup>a</sup>	Band 7 <sup>a</sup>
0208–512	3.24±0.25	3.69±0.30	4.19±0.42	3.81±0.61	2.88±0.79	1.95±1.00	1.51±1.49
0827+243	0.73±0.22	1.03±0.28	1.08±0.36	0.92±0.50	-	-	-
1127–145	2.65±0.34	2.50±0.43	3.21±0.68	3.17±1.05	-	-	-
1510–089	9.74±0.38	10.62±0.48	10.19±0.67	11.57±1.09	7.51±1.47	7.15±2.26	5.14±3.01
3C 454.3	37.22±0.67	39.36±0.91	43.79±1.42	44.20±2.31	26.65±2.96	17.98±3.99	4.55±3.28

<sup>a</sup>Band 1: 200–400 MeV, Band 2: 400–800 MeV, Band 3: 800–1600 MeV, Band 4: 1600–3200 MeV, Band 5: 3200–6400 MeV, Band 6: 6400–12800 MeV, and Band 7: 12800–25600 MeV

411 (IC) emission model described in Tavecchio & Ghisellini (2008), where both synchrotron and  
 412 external (BLR and DT) photons are considered as seed radiation fields contributing to the IC  
 413 process (SSC+ECR). The electron distribution is modeled as a smoothly broken power-law:

$$N'(\gamma) = K \gamma^{-n_1} \left( 1 + \frac{\gamma}{\gamma_{\text{br}}} \right)^{n_1 - n_2}, \quad (1)$$

414 where  $K$  (cm $^{-3}$ ) is a normalization factor,  $n_1$  and  $n_2$  are the energy indices below and  
 415 above the break Lorentz factor  $\gamma_{\text{br}}$ . The electron distribution extends within the limits  
 416  $\gamma_{\text{min}} < \gamma < \gamma_{\text{max}}$ . We also assume that the ‘blazar emission zone’, with the comoving size  $R$   
 417 and magnetic field intensity  $B$ , is located at the distance  $r$  such that  $r_0 < r < r_{\text{BLR}} < r_{\text{DT}}$ ,  
 418 where  $r_0$  is the distance below which the photon energy density in the jet rest frame is  
 419 dominated by the direct radiation of the accretion disk,  $r_{\text{BLR}}$  is the characteristic scale of  
 420 the broad-line-region, and  $r_{\text{DT}}$  is the scale of the dusty torus (see the discussion in Tavecchio  
 421 & Ghisellini 2008 as well as in Sikora et al. 2009). This choice, while somewhat arbitrary,  
 422 has been validated by a number of authors modeling broad-band spectra of FSRQs. Hence,  
 423 the comoving energy density of the dominant photon field — provided by the BLR — is

$$U'_{\text{rad}} \simeq \Gamma_j^2 \frac{\eta_{\text{BLR}} L_d}{4\pi r_{\text{BLR}}^2 c}, \quad (2)$$

424 where  $\Gamma_j$  is the jet bulk Lorentz factor, and the BLR is assumed to reprocess  $\eta_{\text{BLR}} \simeq 10\%$   
 425 of the disk luminosity  $L_d$ . Finally, we assume that the jet viewing angle is in all the cases  
 426  $\theta_j \simeq 1/\Gamma_j$ , so that the jet Doppler factor  $\delta_j \simeq \Gamma_j$ .

427 The results of model fitting are shown in different panels of Figure 7, and the resulting  
 428 parameters are summarized in Table 10. In the context of this model, where we assume the

429 dissipation region to be between the immediate vicinity of the accretion disk but within the  
 430 BLR, it is clear that in all cases the LAT fluxes are dominated by the IC/BLR component,  
 431 while in the X-ray band both IC/BLR and IC/DT processes may contribute at a comparable  
 432 level. In addition, the SSC emission seems negligible, being in particular too weak to ac-  
 433 count for the soft X-ray excess discussed in the previous sections. This excess, on the other  
 434 hand, may be well represented by the high-energy tail of the synchrotron continuum, or an  
 435 additional blackbody-type spectral component.

Table 10: Model parameters used to calculate the SEDs of five FSRQs

Object	$n_1$	$n_2$	$\gamma_{\min}$	$\gamma_{\text{br}}$	$\gamma_{\max}$	$K$ [ $10^4 \text{ cm}^{-3}$ ]	$\Gamma_j$	$R$ [ $10^{16} \text{ cm}$ ]	$B$ [G]	$L_d$ [ $10^{46} \text{ erg/s}$ ]	$r_{\text{BLR}}$ [ $10^{18} \text{ cm}$ ]	$r_{\text{DT}}$ [ $10^{18} \text{ cm}$ ]
0208–512	2	3.3	3.0	700	$4.3 \times 10^4$	2.2	15	1.8	1.1	1.5	0.76	3.0
0827+243	2	3.3	1.5	300	$1.0 \times 10^4$	8.5	10	1.8	3.8	2.0	1.3	4.2
1127–145	2	3.4	1.2	110	$5.0 \times 10^3$	0.65	10	6.5	4.1	10	0.8	10
1510–089	2	3.5	3.0	190	$4.6 \times 10^4$	0.81	13	4	0.8	0.3	0.48	4
3C 454.3	2	3.8	1.0	290	$3.0 \times 10^4$	4.5	12	3.2	0.8	4.0	1.5	30

436 Based on the model results, for each object we compute the ratio of the comoving energy  
 437 densities stored in jet electrons and the magnetic field,

$$\frac{U'_e}{U'_B} = \frac{\int_{\gamma_{\min}}^{\gamma_{\max}} \gamma m_e c^2 N'(\gamma) d\gamma}{B^2/8\pi}, \quad (3)$$

438 where  $B$  is the magnetic field intensity in the emission region. In addition, we compute the  
 439 implied total kinetic jet power as

$$L_j = \pi R^2 c \Gamma_j^2 (U'_e + U'_B + U'_p), \quad (4)$$

440 where  $R$  is the emission region linear size, and  $U'_p$  is the energy density of cold protons.  
 441 The latter parameter is estimated assuming one proton per ten electron-positron pairs (see  
 442 the discussion in Sikora et al. 2009), namely  $U'_p = 0.1 m_p c^2 \int_{\gamma_{\min}}^{\gamma_{\max}} N'(\gamma) d\gamma$ . The resulting  
 443 total kinetic power of the outflow is then compared with the accretion luminosity (assuming  
 444 standard accretion disk with 10% radiative efficiency), by means of the evaluated efficiency  
 445 parameter  $\eta_j = L_j/L_{\text{acc}} \simeq L_j/10 L_d$ , where  $L_d$  is the disk luminosity implied by the model  
 446 fitting (see Table 10). Note that with the above model assumptions and the model parameters  
 447 inferred by us, the jets of objects considered here are dynamically dominated by cold protons,  
 448  $U'_p/U'_e \simeq 200/\langle\gamma\rangle > 1$ , since the mean Lorentz factor of the radiating ultra-relativistic  
 449 electrons is in all the cases  $\langle\gamma\rangle \ll 200$  (see Table 11).

Table 11: Jet parameters of five FSRQs in low-activity states

Object	$U'_e/U'_B$	$L_j$ [ $10^{46}$ erg/s]	$\eta_j$	$\langle\gamma\rangle$
0208–512	2	0.8	0.06	16
0827+243	0.6	2.8	0.14	8
1127–145	0.03	5.8	0.06	5
1510–089	0.9	1	0.35	12
3C 454.3	7	9.4	0.23	5

450 Some of the derived jet parameters for five luminous blazars in their low-activity states  
 451 are significantly different from the analogous parameters claimed for the flaring states, *even*  
 452 *in the same object*. For example, in the case of the high-activity state of PKS 1510–089,  
 453 Kataoka et al. (2008) estimated (under the same assumptions regarding the jet content as in  
 454 this paper) the total kinetic power of the jet as  $L_j \sim 2.7 \times 10^{46} \text{ erg s}^{-1}$ , which is larger than  
 455 the value derived in this paper, by about a factor of 3. In addition, our model values of the  
 456 jet bulk Lorentz factors are also systematically lower than the ones given in the literature  
 457 ( $\Gamma_j \simeq 10$  versus 20). Interestingly, other jet parameters, such as magnetic field intensity  
 458 -  $B \simeq 1 \text{ G}$  - and the equipartition ratio,  $U'_e/U'_B \sim 1$ , or the general spectral shape of the  
 459 electron energy distribution, are comparable to the ones found for flaring FSRQs, (albeit  
 460 with a substantial scatter). It should be noted in this context, however, that for the three  
 461 sources considered in this paper (namely PKS 1127–145, PKS 1510–089, and 3C 454.3), the  
 462 flaring states were analyzed in a framework of the IC/DT model (Błażejowski et al. 2004,  
 463 Kataoka et al. 2008, Sikora et al. 2008, respectively), while here, we argue that the IC/BLR  
 464 contribution is dominant, as motivated by the detected relatively short (day) variability  
 465 timescale of the X-ray continua. On the other hand, as discussed recently in Sikora et al.  
 466 (2009), there is so-called a ‘conspiracy’ between the IC/BLR and IC/DT models, in a sense  
 467 that the resulting inferred jet parameters are comparable in both cases. Hence, we can  
 468 safely conclude that the low- and high-activity states of luminous blazar sources are due  
 469 to the low and high total kinetic power of the jet, respectively, possibly related to varying  
 470 bulk Lorentz factors within the blazar emission zone. And indeed, keeping in mind that the  
 471 highly dynamical and complex jet formation processes in the closest vicinity of supermassive  
 472 black holes – most likely shaped by accretion process subjected to several possible instability  
 473 of the jet fuel, especially when the accretion rate is close to Eddington – such a significant  
 474 variation in the total kinetic output of the outflow should not be surprising. Further support  
 475 for this scenario comes from the fact that the jet efficiency factors estimated here,  $\eta_j \lesssim 1$ ,  
 476 are significantly lower than the ones found for powerful blazars in their flaring states (see  
 477 Sambruna et al. 2006, Ghisellini et al. 2009), even if the difference in the jet proton content

478 adopted by various authors is taken into account.

479

## 4.2. Spectral Evolution

480 As shown in § 3.1.3, the X-ray spectra of the FSRQs analyzed here flatten with increasing  
 481 flux. For  $\Gamma_j \sim \delta_j \sim 10$  and the dominant IC/BLR emission process, the electrons emitting  
 482 the observed 1–10 keV photons have Lorentz factor  $\gamma \sim \gamma_{\min} \sim \text{few}$ . The electrons emitting  
 483 X-ray photons in these sources are very low-energy, so cooling effects cannot play any role  
 484 in the observed spectral evolution. In particular, it can be easily demonstrated that in a  
 485 framework of our model (i.e., for the dominant IC/BLR energy losses), a strong cooling  
 486 regime is expected only for the electrons with Lorentz factors greater than

$$\begin{aligned} \gamma_{\text{cr}} &\simeq \frac{3\pi m_e c^3 r_{\text{BLR}}^2}{\sigma_T R \Gamma_j^2 \eta_{\text{BLR}} L_d} \\ &\simeq 350 \left( \frac{r_{\text{BLR}}}{10^{18} \text{ cm}} \right)^2 \left( \frac{\eta_{\text{BLR}}}{0.1} \right)^{-1} \left( \frac{\Gamma_j}{10} \right)^{-2} \left( \frac{L_d}{10^{46} \text{ erg/s}} \right)^{-1} \left( \frac{R}{10^{16} \text{ cm}} \right)^{-1}. \end{aligned} \quad (5)$$

487 This, for the fitting parameters as given in Table 10, is typically above or just around the  
 488 break Lorentz factor,  $\gamma_{\text{cr}} \gtrsim \gamma_{\text{br}}$  (in agreement with the discussion in Sikora et al. 2009).  
 489 Adiabatic losses, if present, should not result in changing the slope of the power-law X-ray  
 490 continua as well. Thus, one may suspect that the revealed spectral changes are shaped  
 491 by the acceleration process within the blazar emission zone. In the case of relativistic jets  
 492 the relevant acceleration processes are still quite uncertain, although, as pointed out by  
 493 Kataoka et al. (2008) and Sikora et al (2009), the repeatedly observed flat X-ray photon  
 494 indices  $\Gamma \leq 1.5$  seem to favor the mechanism discussed by Hoshino et al. (1992) for the low-  
 495 energy segment of the electron energy distribution. In this model, the low-energy electrons  
 496 (with Lorentz factors, roughly,  $\gamma < m_p/m_e$ ) are accelerated by a resonant absorption of the  
 497 cyclotron emission generated by cold protons reflected from the shock front. As shown later  
 498 by Amato & Arons (2006), the power-law slope of these accelerated electrons depends on  
 499 the relative number of electrons to protons at the shock front. Hence, a larger fraction of  
 500 the energy carried by jet protons during the higher-activity states should in principle result  
 501 in a more efficient acceleration of jet electrons and their flatter spectrum, in agreement with  
 502 the observed X-ray spectral evolution discussed here.

503

The above interpretation, on the other hand, would imply a significant variability in the  
 504  $\gamma$ -ray frequency range. Indeed, the broken power-law form of the electron energy distribution  
 505 revealed by our spectral modeling discussed in the previous section implies the  $\gamma$ -ray flux

506  $F_\gamma \equiv [\nu F_\nu]_\gamma$  around the IC spectral peak  $\nu_\gamma \sim 10^{22}$  Hz should be, roughly

$$F_\gamma \simeq F_X \left( \frac{\nu_\gamma}{\nu_X} \right)^{2-\Gamma} \simeq 10^{4(2-\Gamma)} F_X, \quad (6)$$

507 where  $F_X$  is the monochromatic X-ray flux measured around  $\nu_X \sim 10^{18}$  Hz, and  $\Gamma$  is the  
 508 observed X-ray photon index. For example, our analysis for PKS 0208–512 indicates a  
 509 photon index  $\Gamma_1 \sim 1.8$  for an X-ray flux  $F_{X,1} \sim 1.2 \times 10^{-12}$  erg cm<sup>-2</sup> s<sup>-1</sup> in the lower state,  
 510 and  $\Gamma_2 \sim 1.5$  for  $F_{X,2} \sim 1.6 \times 10^{-12}$  erg cm<sup>-2</sup> s<sup>-1</sup> in the higher state. Thus, if the observed X-  
 511 ray variability is due to flattening of the electron energy distribution during the acceleration  
 512 process, one should observe the  $\gamma$ -ray variability of the order of

$$\frac{F_{\gamma,2}}{F_{\gamma,1}} \simeq 10^{4(\Gamma_1-\Gamma_2)} \frac{F_{X,2}}{F_{X,1}} \sim 20. \quad (7)$$

513 However, during the simultaneous *Fermi* observation, no significant  $\gamma$ -ray variability was  
 514 observed for the analyzed sources, at least within one day timescale.

515 Therefore, the most viable explanation for the observed X-ray spectral evolution is that  
 516 the IC power-law slope remains roughly constant during the flux variations, but the amount  
 517 of contamination from the additional soft X-ray component increases at low flux levels,  
 518 affecting the spectral fitting parameters at higher photon energies ( $> 2$  keV). Note that in  
 519 such a case the expected gamma-ray variability should be of the same order as the X-ray  
 520 variability, namely  $F_{\gamma,2}/F_{\gamma,1} \simeq F_{X,2}/F_{X,1} \sim 1.3$ .

521 We finally note in this context that, as shown in §3.1.2, the previous BeppoSAX data  
 522 for PKS 0208–512 collected during the high state indicated a convex X-ray spectrum, and  
 523 an excess absorption below 1 keV with a column density of  $N_{\text{H}} \sim 1.67 \times 10^{21}$  cm<sup>-2</sup> exceeding  
 524 the Galactic value by more than a factor of 5. However, the X-ray photon index was similar  
 525 to the one implied by our *Suzaku* observations ( $\Gamma \sim 1.7$ ). Therefore, the convex spectrum  
 526 observed by BeppoSAX may reflect an intrinsic shape of the IC emission involving the low-  
 527 energy cut-off in the electron energy distribution around  $\gamma \sim 1$ , as expected in the EC/BLR  
 528 model (Tavecchio et al. 2007), which is only diluted during the low-activity states due to  
 529 the presence of an additional soft X-ray spectral component.

530 Similar trend has been observed in 3C 454.3. To illustrate this, in Figure 8 we selected  
 531 the data which have a similar power-law slope ( $\Gamma \sim 1.6$ ) and plotted the absorption column  
 532 versus 2–10 keV flux densities derived from the *Chandra* (Villata et al. 2006), *Swift* (Giommi  
 533 et al. 2006), *XMM-Newton* (Raiteri et al. 2007, 2008), and *Suzaku* (this work) observations.  
 534 We can see that there is a trend of increasing the absorption value with source brightness, as  
 535 previously reported by Raiteri et al. (2007; 2008). These results may again be explained by

536 the soft excess emission being more important when the source gets fainter, and becoming  
 537 almost completely “hidden” behind the hard X-ray power-law when the source gets brighter.

538 From the spectral fitting of the *Suzaku* data, we showed in §3.1.2 that the soft X-ray  
 539 excess may be represented either by a steep power-law ( $\Gamma \sim 3 - 5$ ) or a blackbody-type  
 540 emission ( $kT \sim 0.1 - 0.2$  keV). Since the synchrotron peak of each source is located around  
 541 optical photon energies (see Figure 7), the high-energy synchrotron tail may possibly account  
 542 for the observed soft X-ray excess emission, especially if being modified by the Klein-Nishina  
 543 effects (see the discussion in Sikora et al. 2009 and Kataoka et al. 2008). On the other hand,  
 544 the bulk-Compton spectral component produced by Comptonization of the UV accretion  
 545 disk by cold electrons in the innermost parts of relativistic jets (e.g., Begelman & Sikora  
 546 1987) is a natural explanation for the apparent soft X-ray excess component.

## 547 5. Conclusions

548 We have presented the observations and analysis of the data for the  $\gamma$ -ray-loud blazars,  
 549 PKS 0208–512, Q 0827+243, PKS 1127–145, PKS 1510–089, and 3C 454.3, obtained with  
 550 the *Suzaku*, *Swift* UVOT and *Fermi* LAT. Observations were conducted between 2008 Octo-  
 551 ber and 2009 January. These observations allowed us to construct broadband spectra of the  
 552 sources in the low  $\gamma$ -ray activity state, covering optical to GeV photon energy range. Our  
 553 results are as follows:

- 554 1. The X-ray spectra of five FSRQs are well represented by an absorbed hard power-law  
 555 model ( $\Gamma \sim 1.4 - 1.7$ ). For PKS 0208–512, PKS 1127–145, and 3C 454.3, the fitted  
 556 absorption column is larger than the Galactic value (but we note that the “excess  
 557 absorption” is not a unique representation of X-ray spectra of those blazars). Com-  
 558 pared with previous X-ray observations, we see a trend of increasing apparent X-ray  
 559 absorption column with increasing high-energy luminosity of the source.
- 560 2. *Suzaku* observations reveal spectral evolution of the X-ray emission: the X-ray spec-  
 561 trum becomes harder as the source gets brighter. Such spectral changes are most  
 562 likely due to the underlying and steady low-energy spectral component which becomes  
 563 prominent when the inverse-Compton emission gets fainter. This soft X-ray excess can  
 564 be explained as a contribution of the high-energy tail of the synchrotron component,  
 565 or bulk-Compton radiation.
- 566 3. We adopt the location of the blazar emission region to be outside of the immediate  
 567 vicinity of the accretion disk but within the BLR, and within the context of this

568 model, we find that the contribution of the synchrotron self-Compton process to the  
569 high-energy radiative output of FSRQs is negligible even in their low-activity states.

- 570 4. We argue that the difference between the low- and high-activity states in luminous  
571 blazars is due to the different total kinetic power of the jet, most likely related to  
572 varying bulk Lorentz factor of the outflow within the blazar emission zone.

573 The *Fermi* LAT Collaboration acknowledges generous ongoing support from a number  
574 of agencies and institutes that have supported both the development and the operation of the  
575 LAT as well as scientific data analysis. These include the National Aeronautics and Space  
576 Administration and the Department of Energy in the United States, the Commissariat à  
577 l’Energie Atomique and the Centre National de la Recherche Scientifique / Institut National  
578 de Physique Nucléaire et de Physique des Particules in France, the Agenzia Spaziale Italiana  
579 and the Istituto Nazionale di Fisica Nucleare in Italy, the Ministry of Education, Culture,  
580 Sports, Science and Technology (MEXT), High Energy Accelerator Research Organization  
581 (KEK) and Japan Aerospace Exploration Agency (JAXA) in Japan, and the K. A. Wallen-  
582 berg Foundation, the Swedish Research Council and the Swedish National Space Board in  
583 Sweden.

584 Additional support for science analysis during the operations phase is gratefully acknowl-  
585 edged from the Istituto Nazionale di Astrofisica in Italy and the Centre National d’Études  
586 Spatiales in France.

587 LS was partially supported by the Polish Ministry of Science and Higher Education  
588 through the project N N203 380336.

## 589 REFERENCES

- 590 Abdo, A. A., et al. 2009a, *ApJS*, 183, 46  
591 Abdo, A. A., et al. 2009b, *ApJ*, 700, 597  
592 Abdo, A. A., et al. 2009c, *ApJ*, 699, 31  
593 Abdo, A. A., et al. 2010, *ApJ*, 710, 1271  
594 Amato, E., & Arons, J. 2006, *ApJ*, 653, 325  
595 Atwood, W. B., et al. 2009, *ApJ*, 697, 1071

- 596 Barthelmy, S. D., et al. 2005, *Space Sci. Rev.*, 120, 143
- 597 Błażejowski, M., Sikora, M., Moderski, R., & Madejski, G. M. 2000, *ApJ*, 545, 107
- 598 Błażejowski, M., Siemiginowska, A., Sikora, M., Moderski, R., & Bechtold, J. 2004, *ApJ*,  
599 600, L27
- 600 Burrows, D. N., et al. 2005, *Space Sci. Rev.*, 120, 165
- 601 Bechtold, J., Siemiginowska, A., Aldcroft, T. L., Elvis, M., & Dobrzycki, A. 2001, *ApJ*, 562,  
602 133
- 603 Begelman, M. C., & Sikora, M. 1987, *ApJ*, 322, 650
- 604 Cardelli, J. A., Clayton, G. C., & Mathis, J. S. 1989, *ApJ*, 345, 245
- 605 Celotti, A., Ghisellini, G., & Fabian, A. C. 2007, *MNRAS*, 375, 417
- 606 Dermer, C. D., & Schlickeiser, R. 1993, *ApJ*, 416, 458
- 607 Dickey, J. M., & Lockman, F. J. 1990, *ARA&A*, 28, 215
- 608 Donato, D., Sambruna, R. M., & Gliozzi, M. 2005, *A&A*, 433, 1163
- 609 Donnarumma, I., et al. 2010, submitted to *ApJ*
- 610 Edelson, R., Griffiths, G., Markowitz, A., Sembay, S., Turner, M. J. L., Warwick, R. 2001,  
611 *ApJ*, 554, 274
- 612 Foschini, L., et al. 2006, *A&A*, 453, 829
- 613 Fukazawa, Y., et al. 2006, *Proc.SPIE*, 6266, 75
- 614 Ghisellini, G., Celotti, A., Fossati, G., Maraschi, L., & Comastri, A. 1998, *MNRAS*, 301,  
615 451
- 616 Ghisellini, G., Tavecchio, F., & Ghirlanda, G. 2009, *arXiv:0906.2195*
- 617 Giommi, P., et al. 2006, *A&A*, 456, 911
- 618 Hill, J., et al. 2004, *APS*, 10005H
- 619 Hoshino, A., Arons, J., Gallant, Y. A., & Langdon, A. B. 1992, *ApJ*, 390, 454
- 620 Hartman, R. C., et al. 1999, *ApJS*, 123, 79

- 621 Jorstad, S. G., & Marscher, A. P. 2004, ApJ, 614, 615
- 622 Kataoka, J., et al. 1999, ApJ, 514, 138
- 623 Kataoka, J., et al. 2008, ApJ, 672, 787
- 624 Kokubun, M. et al. 2007, PASJ, 59, S53
- 625 Koyama, K. et al. 2007, PASJ, 59, S23
- 626 Maraschi, L., Ghisellini, G., and Celotti, A. 1992, ApJ, 397, L5
- 627 Mitsuda, K. et al. 2007, PASJ, 59, S1
- 628 Moderski, R., Sikora, M., Madejski, G. M., & Kamae, T. 2004, ApJ, 611, 770
- 629 Mukherjee, R. et al. 1999, ApJ, 527, 133
- 630 Murphy, E. M., Lockman, F. J., Laor, A., & Elvis, M. 1996, ApJS, 105, 369
- 631 Raiteri, C. M., et al. 2007, A&A, 473, 819
- 632 Raiteri, C. M., et al. 2008, A&A, 491, 755
- 633 Roming, P. W. A., et al. 2005, Spacs Sci. Rev., 120, 95
- 634 Poole, T. S., et al. 2008, MNRAS, 383, 627
- 635 Sambruna, R. M., et al. 1997, ApJ, 474, 639
- 636 Sambruna, R. M., Gliozzi, M., Tavecchio, F., Maraschi, L., & Foschini, L. 2006, ApJ, 652,  
637 146
- 638 Serlemitsos, P. J., et al. 2007, PASJ, 59, S9
- 639 Sikora, M., Begelman, M. C., & Rees, M. J., 1994, ApJ, 421, 153
- 640 Sikora, M., & Madejski, G. M. 2000, ApJS, 534, 109
- 641 Sikora, M., Moderski, R., & Madejski, G. M. 2008, ApJ, 675, 71
- 642 Sikora, M., Stawarz, L., Moderski, R., Nalewajko, K., & Madejski, G. 2009, ApJ, 704, 38
- 643 Sokolov, A., & Marscher, A.P. 2005, ApJ, 629, 52
- 644 Takahashi, T. et al. 2007, PASJ, 59, S35

- 645 Tavecchio, F., et al. 2000, ApJ, 543, 535
- 646 Tavecchio, F., et al. 2002, ApJ, 575, 137
- 647 Tavecchio, F., Maraschi, L., Ghisellini, G., Kataoka, J., Foschini, L., Sambruna, R. M., &  
648 Tagliaferri, G. 2007, ApJ, 665, 980
- 649 Tavecchio, F., & Ghisellini, G. 2008, MNRAS, 386, 945
- 650 Thompson, D. J., et al. 1993, ApJS, 86, 629
- 651 Villata, M., et al. 2006, A&A, 453, 817

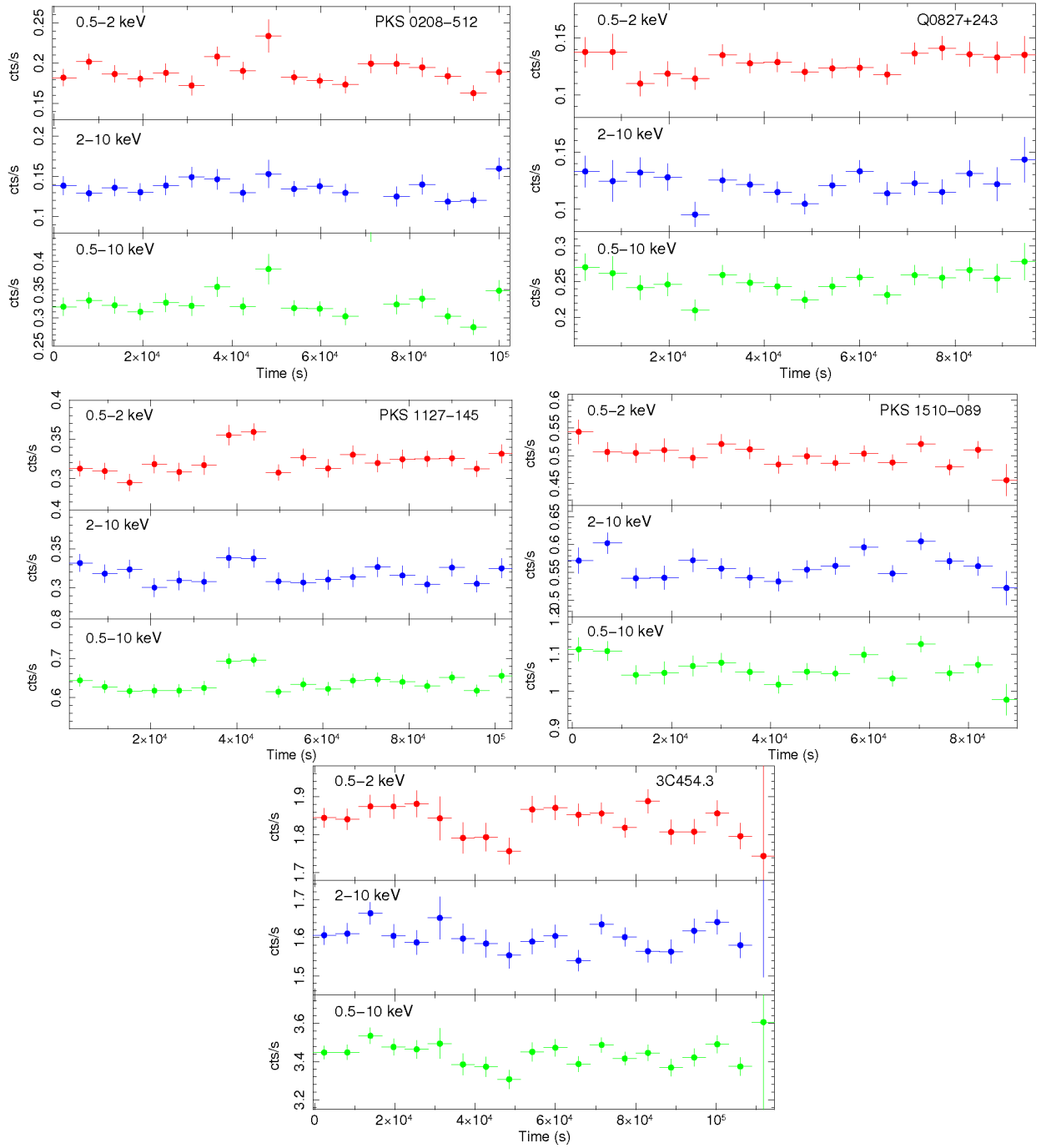


Fig. 1.— Light curves of five FSRQs: 0.5 – 2 keV (*upper panels*), 2 – 10 keV (*middle panels*), and 0.5 – 10 keV (*bottom panels*). All the light curves were binned at 5760 s, corresponding to the period of the *Suzaku* orbit.

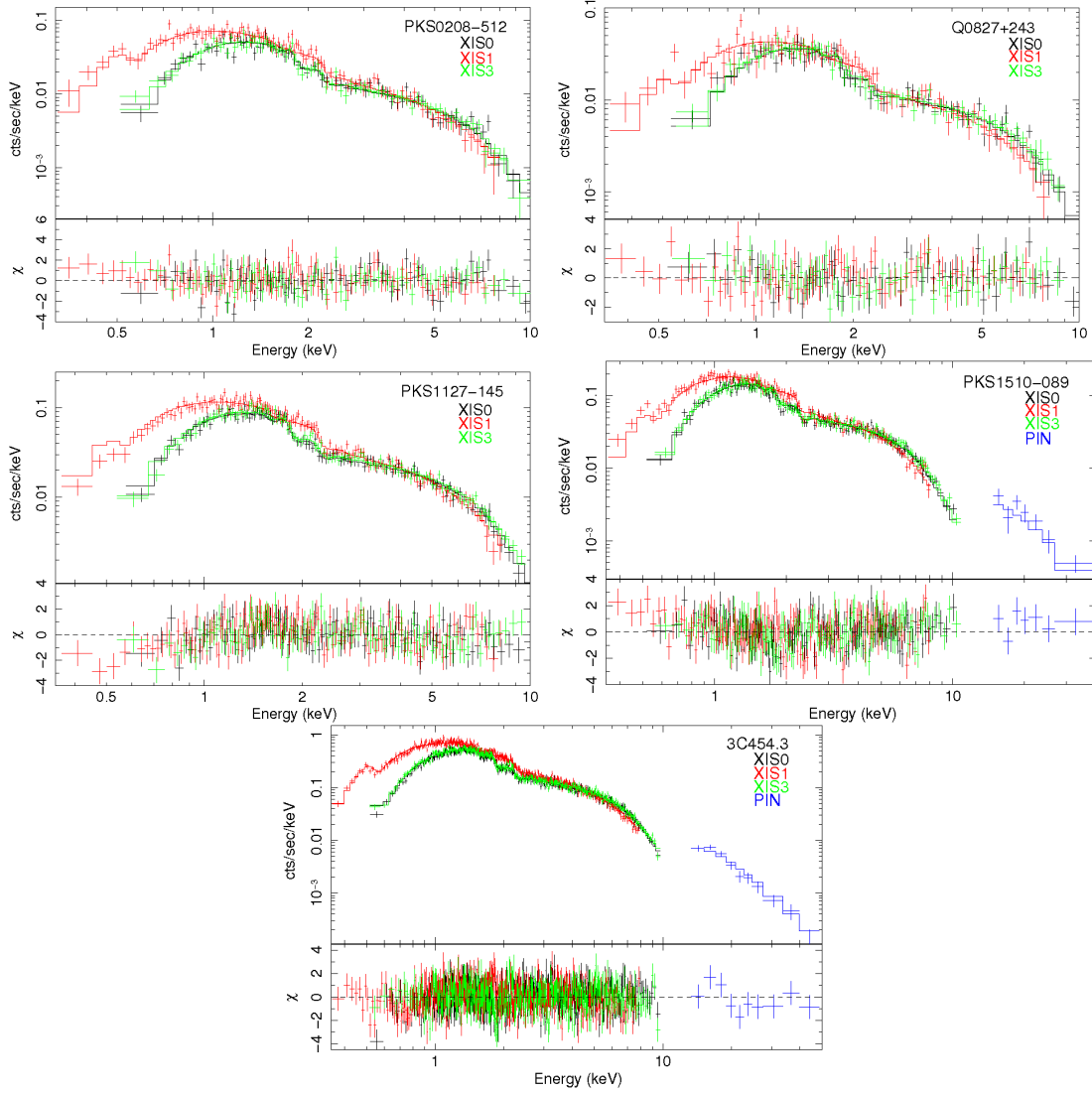


Fig. 2.— *Suzaku* spectra of five FSRQs: the top panel shows the data, plotted against a power-law model with the Galactic absorption. The bottom panel shows the residuals for the power-law fit. For 0208–512 and 1510–089, the data below 1 keV are in excess to the model. On the other hand, for 1127–145, the residuals show a substantial deficit of photons at low energies. For 3C454.3, some scatter around 1 keV in the residual panel is seen.

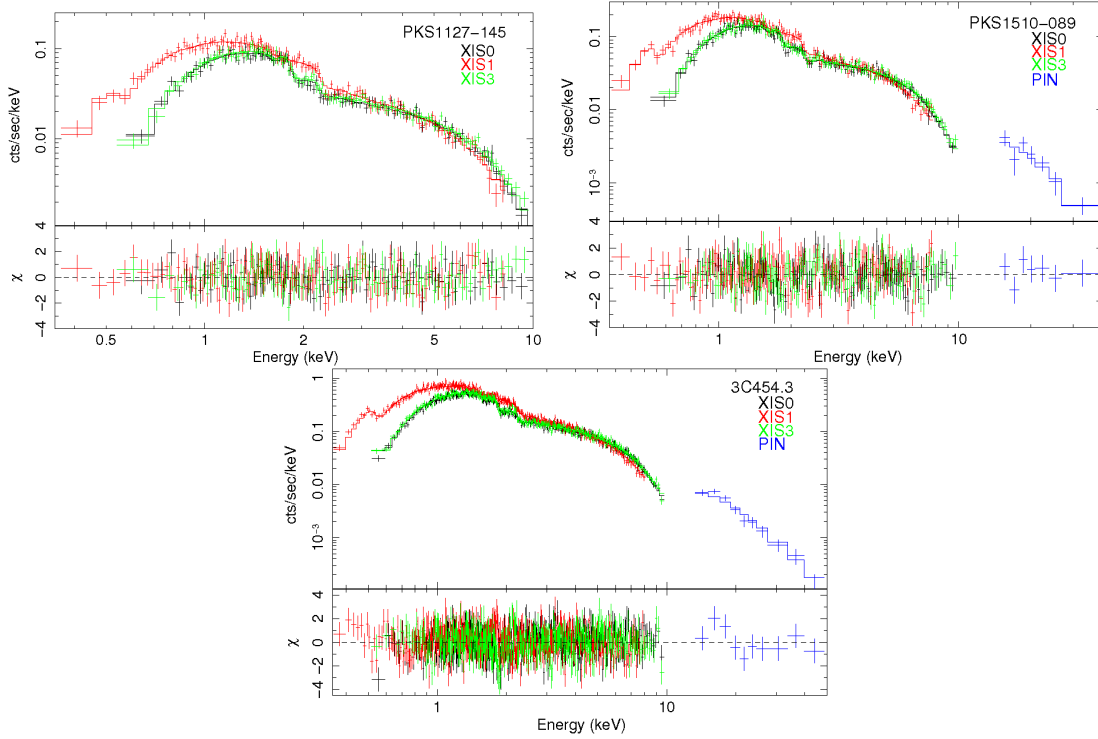


Fig. 3.— Best fit *Suzaku* spectrum of PKS 1127–145, PKS 1510–089 and 3C454.3. The top panel shows the data, plotted against an absorbed power-law model. The bottom panel shows the residuals to the power-law fit.

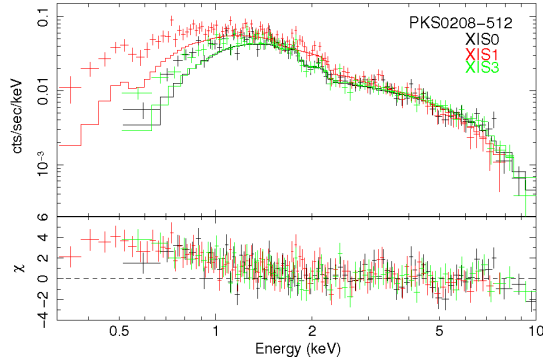


Fig. 4.— *Suzaku* spectrum of PKS 0208–512, with residuals assuming a column density of  $N_{\text{H}} \sim 1.67 \times 10^{21} \text{ cm}^{-2}$ . Deviations due to soft excess emission can be clearly seen.

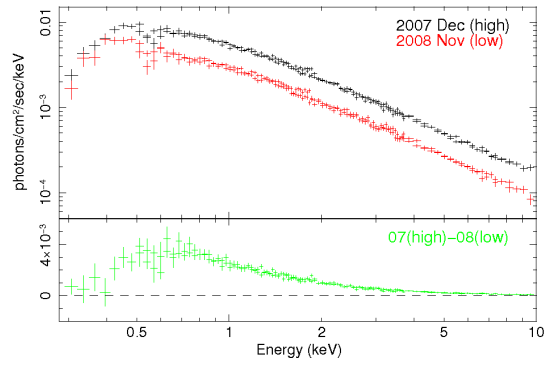


Fig. 5.— Unfolded spectra of 3C 454.3 obtained in 2007 (high) and 2008 (low), respectively. The bottom panel shows the residuals by subtracting the spectra in the high state from those in the low state.

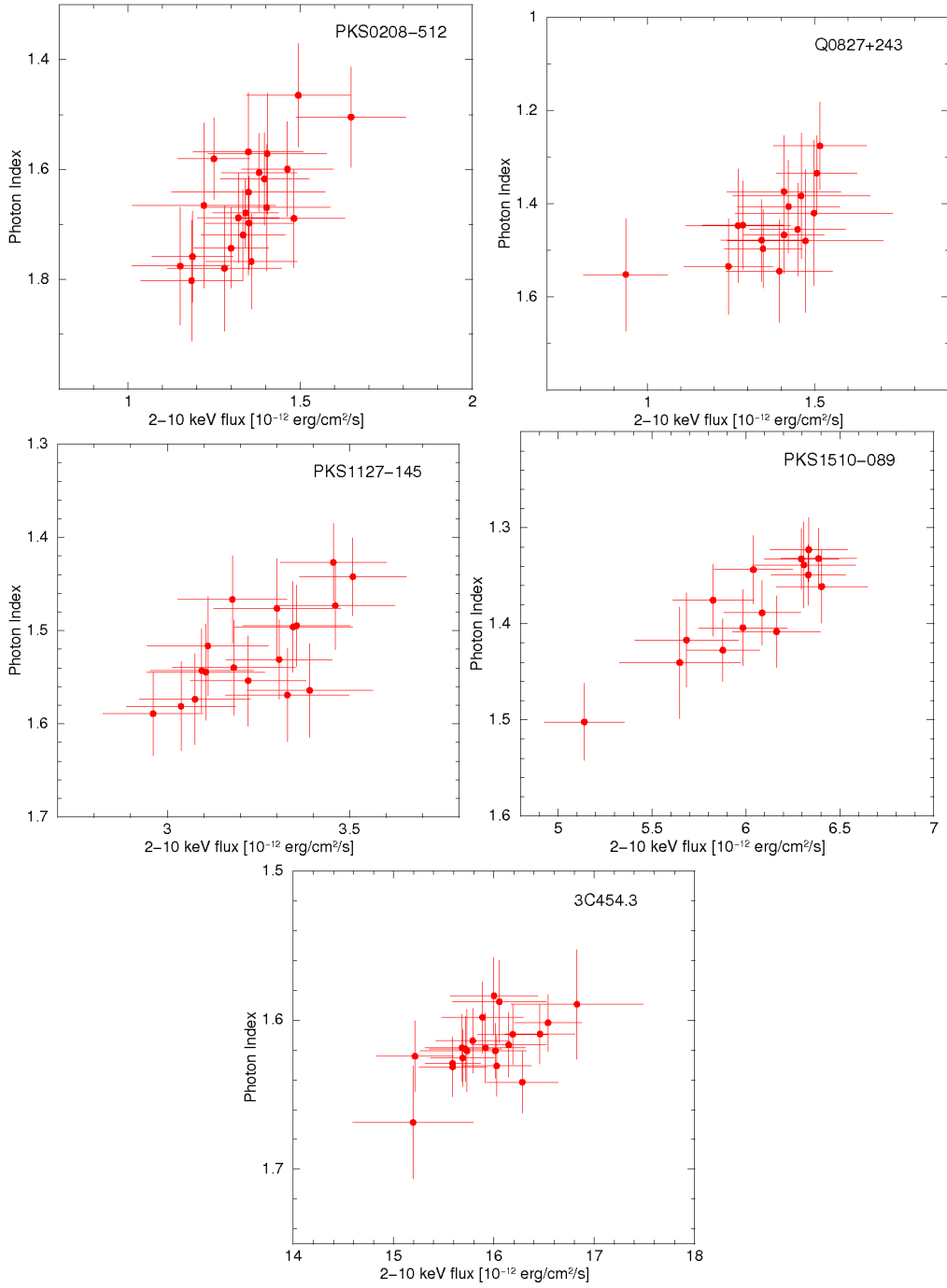


Fig. 6.— Correlation of the 2 – 10 keV flux vs. photon index of five blazars as measured by the *Suzaku* XISs.

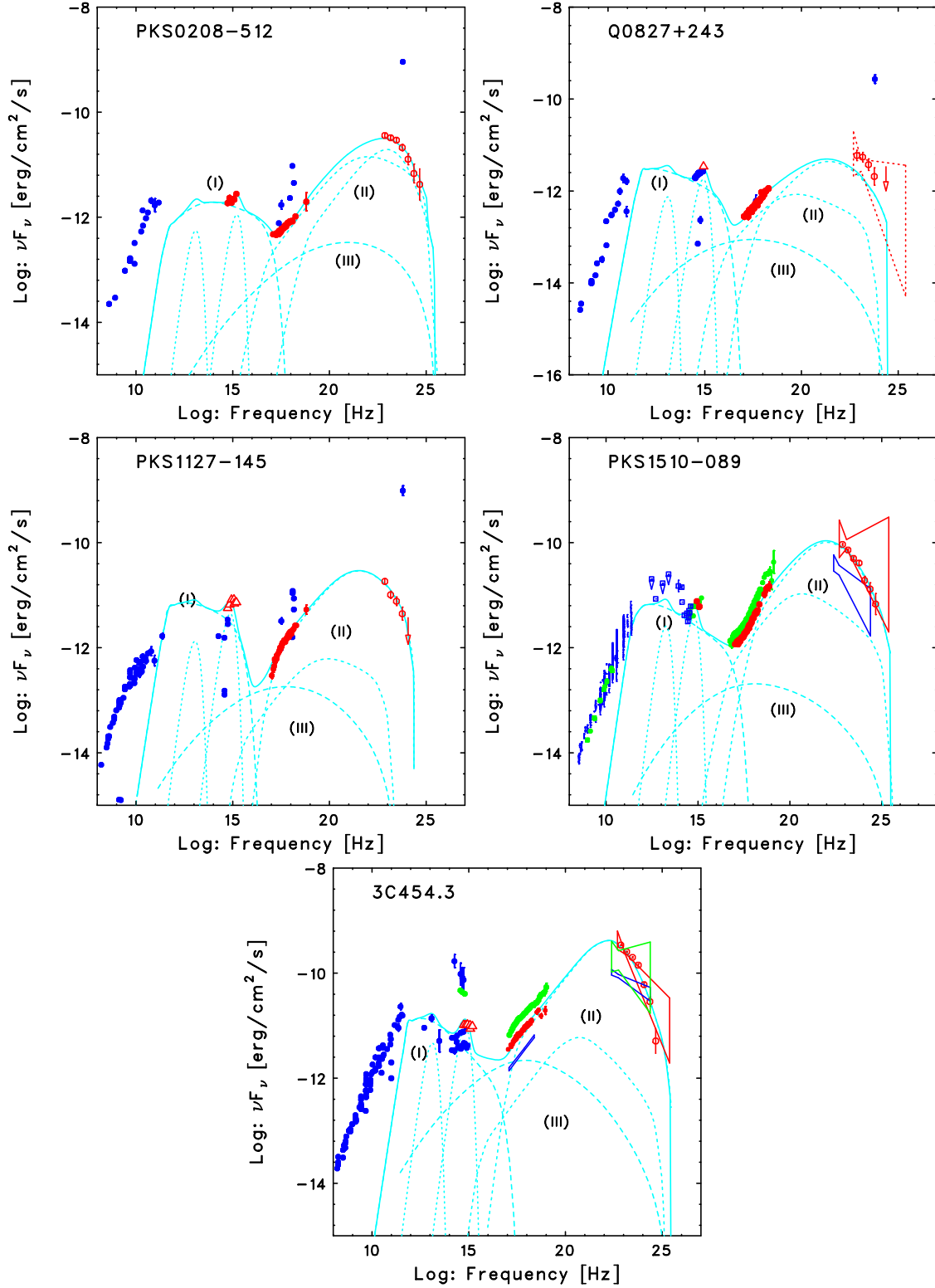


Fig. 7.— Overall SED of five sources constructed with broad-band data obtained during 2008 October to 2009 January (filled red circles and solid bow-tie). Quasi simultaneous data are also shown (open red circles). Historical radio (NED) and  $\gamma$ -ray (EGRET) data are also plotted as filled blue circles. Green symbols in the SEDs of PKS 1510–089 and 3C454.3 denote the previous simultaneous observations (Kataoka et al. 2008; Donnarumma et al. 2010). The dotted lines show (I) the synchrotron and (II) the EC components, and (III)

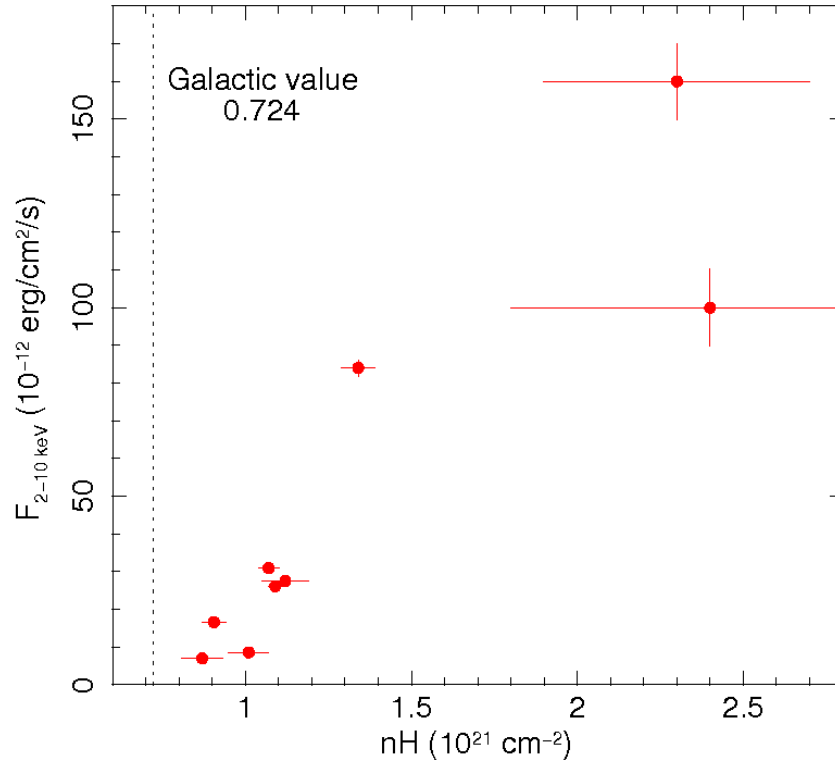


Fig. 8.— Fluxes in the 2 – 10 keV band for different observations of 3C 454.3 vs.  $N_H$  for the fits with an absorbed power-law model. The dashed line indicates the Galactic absorption column. This figure indicates that the intrinsic X-ray spectrum is not a simple power-law, but instead, it shows some curvature, which may depend on the X-ray brightness.